Continuation-based Computation of Global Isochrons[*]

Hinke M. Osinga[†] and Jeff Moehlis[‡]

Abstract. Isochrons are foliations of phase space that extend the notion of phase of a stable periodic orbit to the basin of attraction of this periodic orbit. Each point in the basin of attraction lies on only one isochron, and two points on the same isochron converge to the periodic orbit with the same phase. Global isochrons, that is, isochrons extended into the full basin of attraction rather than just a neighborhood of the periodic orbit, can form remarkable foliations. For example, accumulations of all isochrons can occur in arbitrarily small regions of phase space; the limit of such an accumulation is called the phaseless set, which lies on the boundary of the basin of attraction of the periodic orbit. Since global isochrons must typically be approximated numerically, such complicated geometries are often difficult to realize for actual examples. Indeed, the computation of global isochrons can be challenging, particularly for systems with multiple time scales. We present a novel method for computing isochrons via the continuation of a two-point boundary value problem, which is particularly effective for systems with multiple time scales. We use this method to compute global isochrons for a two-dimensional reduced Hodgkin–Huxley model and illustrate that the one-dimensional isochrons for a planar multiple-time-scale system can accumulate in the interior of the basin of attraction of the periodic orbit in a way similar to two-dimensional isochrons accumulating on the boundary of a three-dimensional basin of attraction.

Key words. isochron, phase response curve, Hodgkin–Huxley, two-point boundary value problem, continuation method

AMS subject classifications. 37C10, 65P99, 37N25

DOI. 10.1137/090777244

1. Introduction. Many biological systems produce rhythmic oscillations that are self-sustained, with an internal source of energy being transformed into oscillations of chemical concentrations and electrical and mechanical properties. Such biological oscillators have a long, successful history of being modeled using ordinary differential equations [27, 29]. A prototypical example of a biological oscillator is the stable periodically firing action potential generated by the giant axon of a squid for a range of constant bias currents [26]. This behavior was famously modeled by Hodgkin and Huxley [26] using a four-dimensional system of coupled nonlinear ordinary differential equations, representing the voltage difference across a neural membrane and three gating variables related to ionic flow across the membrane.

A powerful technique for analyzing a biological oscillator is the rigorous reduction to a phase model, with a single variable describing the phase of the oscillation with respect to some

reference state; see, for example, [4, 21]. This tremendous reduction in the dimensionality and complexity of a system often retains enough information to yield a useful understanding of its dynamics. Moreover, the analysis of the system is greatly simplified, because phase models tend to depend on only a very small number of parameters [4]. Such a reduction to a phase model is based on the notion of *isochrons* of the oscillator for the system. The concept of isochrons of a stable periodic orbit Γ (the oscillator) was first introduced by Winfree [45] in 1974. In that paper he provides formal definitions that we reformulate in the next section. In words, isochrons are (codimension-one) manifolds of initial conditions in phase space, with the property that all solution trajectories that correspond to initial conditions on the same isochron asymptotically approach Γ at the same phase [45]. Hence, isochrons are defined relative to Γ and make sense only for points in its basin of attraction $\mathcal{B}(\Gamma)$. The phase-dependent family of isochrons gives a sense of how long a trajectory spends in different regions of phase space: for example, a trajectory moves slowly through regions of state space where isochrons that are equally spaced in phase lie relatively close to each other. Winfree poses a number of conjectures in [45] and, in particular, wonders about the geometry of isochrons at the boundary $\partial \mathcal{B}(\Gamma)$ of $\mathcal{B}(\Gamma)$. He argues that, under suitable genericity conditions, each isochron must come arbitrarily close to any point on $\partial \mathcal{B}(\Gamma)$, which he calls the *phaseless set* [45, appendix, Conjecture C]. Guckenheimer provides proofs of these conjectures in [21] and illustrates them with several examples; in particular, he gives an example [21, Figure 4] that illustrates Conjecture C in a three-dimensional phase space and explains how this inevitably leads to very complicated geometries of the (two-dimensional) limits of the isochrons on $\partial \mathcal{B}(\Gamma)$.

In this paper we present a two-dimensional example with a unique globally attracting periodic orbit Γ for which the associated one-dimensional isochrons foliate the phase space in a remarkably complicated way that is manifest only in the *interior* of $\mathcal{B}(\Gamma)$. Indeed, the complex geometry of the limits of isochrons on $\partial \mathcal{B}(\Gamma)$, as predicted and illustrated by Guckenheimer, can occur only in three dimensions. We show that similar complex structures can be realized (and readily visualized) in a planar phase space of a system with multiple time scales; if the ratio between the time scales is sufficiently small, then the isochrons interact with a bounded set of points similar to a phaseless set in the interior of $\mathcal{B}(\Gamma)$. In order to find these isochrons, we present a new method for computing global isochrons that is based on the continuation of a suitably posed two-point boundary value problem (BVP); we refer to [10] for an introduction to the continuation of BVPs. With the exception of simple examples, isochrons cannot be calculated analytically, and one has to resort to numerical approximations. An important advantage of our method is the fact that we compute each isochron via continuation, which automatically provides an arclength parameterization of it that organizes phase space according to the notion of arclength distance to Γ. With this method we are able to compute many isochrons and show their detailed structure as each accumulates onto an equilibrium, which is the only point not contained in $\mathcal{B}(\Gamma)$.

This paper is organized as follows. In the next section we give formal definitions and present a brief overview of existing computational methods for finding linear or higher-order local approximations. We specifically focus on a BVP set-up to obtain linear approximations of the isochrons, and describe in section 3 how to use these to compute global isochrons via continuation of a BVP. We provide a pseudocode implementation that performs the computations using the software package AUTO [11] and briefly discuss the accuracy of the

method. Section 4 presents the planar example that exhibits complexity similar to that illustrated by Guckenheimer near the basin boundary for a three-dimensional system. We use the dynamical system considered in [29, 34] for a two-dimensional reduction of the Hodgkin–Huxley model. We are able to compute global isochrons up to such detail that we not only visualize Winfree's Conjecture C [45], but can also analyze the complicated structure in the interior of $\mathcal{B}(\Gamma)$. We end with a discussion in section 5.

2. Definitions and background. Let us begin with a precise definition of an isochron. Consider an autonomous vector field

$$(2.1) \qquad\qquad \frac{d\mathbf{x}}{dt} = F(\mathbf{x}),$$

with solutions $\mathbf{x} = \mathbf{x}(t)$ that satisfy $\mathbf{x}(0) = \mathbf{x}_0 \in \mathbb{R}^n$; here, $\mathbb{R}^n$ is the phase space of (2.1). In this paper we consider planar vector fields, that is, $n = 2$, so that the isochrons are one-dimensional. In principle, it is not essential to have $n = 2$ in what follows, and we come back to this in section 5. We assume that F is sufficiently smooth; that is, F is at least C^1. The vector field (2.1) induces a flow $\Phi : \mathbb{R} \times \mathbb{R}^n \to \mathbb{R}^n$, and we will use the notation $\Phi(t, \mathbf{x}_0) = \Phi^t(\mathbf{x}_0)$. We further assume that (2.1) has an orbit Γ with period T_Γ and that Γ is a hyperbolic attractor; that is, all Floquet multipliers of Γ lie inside the complex unit circle, except for the trivial multiplier 1 associated with the direction tangent to Γ. We associate a phase with points on Γ as follows. Let $\gamma_0 \in \Gamma$ be the point where the phase is zero; here we choose γ_0 to be the global maximum of Γ with respect to the first coordinate. Then $\Gamma = \{\Phi(t, \gamma_0) \mid 0 \leq t < T_\Gamma\}$, and a point $\gamma_t = \Phi(t, \gamma_0)$ has phase $\theta(\gamma_t) = t/T_\Gamma$. The phase $\theta(\gamma_t)$ takes values in $[0, 1)$, which follows the definition by Winfree [45], but other conventions, such as $[0, 2\pi)$ or $[0, T_\Gamma)$, can easily be obtained via rescaling.

Isochrons are closely related to an extended notion of phase that is also defined for points that do not lie on Γ, as follows.

Definition 2.1 (asymptotic phase). *Let $\mathbf{x}_0 \in \mathbb{R}^n$ be an initial condition for* (2.1) *that lies inside the basin of attraction of Γ. Then the unique asymptotic phase $\theta(\mathbf{x}_0)$ of $\mathbf{x}_0$ is given by the condition*

$$\lim_{t \to \infty} \|\Phi(t, \mathbf{x}_0) - \Phi(t + \theta(\mathbf{x}_0)\, T_\Gamma, \gamma_0)\| = 0.$$

Hence, the orbit through $\mathbf{x}_0$ converges asymptotically to Γ in such a way that it will be in phase with the point $\Phi(\theta(\mathbf{x}_0)\, T_\Gamma, \gamma_0)$ on Γ.

The asymptotic phase (which Winfree calls the latent phase) is defined only for points $\mathbf{x}_0 \in \mathbb{R}^n$ that lie in the basin $\mathcal{B}(\Gamma)$ of Γ. If Γ is a global attractor of a planar vector field, then $\mathcal{B}(\Gamma)$ is the entire phase space, with the exception of one or possibly more unstable equilibria. The complement of $\mathcal{B}(\Gamma)$ is also called the *phaseless set* of Γ.

Definition 2.2 (isochron). *An isochron is a level set of the asymptotic phase function $\theta :$ $\mathcal{B}(\Gamma) \subset \mathbb{R}^n \to [0, 1)$, that is, the collection of all points in the basin of attraction of Γ with the same asymptotic phase. We tend to associate isochrons with their corresponding phase points on Γ. More precisely, for $\gamma \in \Gamma$,*

$$\mathcal{I}(\gamma) = \{\mathbf{x}_0 \in \mathcal{B}(\Gamma) \mid \theta(\mathbf{x}_0) = \theta(\gamma)\}.$$

Definition 2.1 implies that isochrons map to each other under the flow; that is, with a slight abuse of notation,

$$(2.2) \qquad\qquad \mathcal{I}(\Phi^t(\gamma_0)) = \Phi^t(\mathcal{I}(\gamma_0)).$$

In particular, each isochron $\mathcal{I}(\gamma)$ is invariant under the time-T_Γ map $\Phi^{T_\Gamma}(\cdot)$, which has γ as its fixed point.

We want to consider isochrons from a dynamical systems point of view. We may think of Γ as a normally hyperbolic manifold, because we assume that only its trivial Floquet multiplier lies on the complex unit circle. Then the tangent bundle of $\mathbb{R}^n$ over Γ can be split into a linear bundle tangent to Γ and a linear stable normal bundle transverse to Γ that is invariant under the linearization of the flow. Moreover, we can define vector directions associated with these two tangent bundles in the tangent space of $\mathbb{R}^n$ at γ for each point $\gamma \in \Gamma$. Since Γ is a periodic orbit, it is easy to find these vector directions: γ is a fixed point of the time-T_Γ map $\Phi^{T_\Gamma}(\cdot)$, and the tangent and normal vector directions are the eigenvectors of the Jacobian matrix $D\Phi^{T_\Gamma}(\gamma)$ associated with the trivial and nontrivial Floquet multipliers, respectively. The local theory of normally hyperbolic, invariant, compact manifolds [25, section 4, Theorem 4.1] ensures the existence of an n-dimensional stable manifold $W^s(\Gamma) = \mathcal{B}(\Gamma)$ that is invariantly foliated by $(n-1)$-dimensional submanifolds $W^{ss}(\gamma)$, $\gamma \in \Gamma$, that are as smooth as the function F that defines (2.1). Moreover, $W^s(\Gamma)$ is tangent to the linear stable normal bundle of Γ, and each $W^{ss}(\gamma)$ is tangent to the corresponding linear stable eigenspace at γ. By definition, $\mathcal{I}(\gamma) = W^{ss}(\gamma)$, $\gamma \in \Gamma$; see [21, 25, 45].

The interpretation of $\mathcal{I}(\gamma)$ as a leaf $W^{ss}(\gamma)$ of the invariant foliation of $W^s(\Gamma)$ offers a natural way of computing isochrons as stable manifolds, which is precisely the approach that we take in this paper. Our method is based on the idea of computing stable manifolds via the continuation of orbit segments [15, 31], which assumes knowledge of the periodic orbit Γ as well as the linear approximation of the stable manifold. Before explaining our method, we summarize in the next section several methods for obtaining *local* approximations of the isochrons.

2.1. Linear approximations of isochrons. The development of computational methods for isochrons has mainly focused on their linear approximations [17, 18, 46]. Indeed, the linear approximation suffices for computing the so-called infinitesimal phase response curve (PRC). To our knowledge Guillamon and Huguet [22] are the first to use higher-order approximation methods for the local approximation of isochrons. We briefly discuss these methods here but primarily focus on the approach that we take for the computations in this paper.

The so-called direct method is based on the formal definition for the infinitesimal PRC. Since $\mathcal{I}(\gamma)$ is a level set of the asymptotic phase θ, we know that the gradient $\nabla\theta(\gamma)$ evaluated at the base point γ is perpendicular to the tangent of $\mathcal{I}(\gamma)$ at γ; this gradient is equal to the infinitesimal PRC [38]. The gradient $\nabla\theta(\gamma)$ is given by the limits

$$\frac{\partial \theta}{\partial x_i}(\gamma) = \lim_{\Delta x_i \to 0} \frac{\theta(\gamma + \Delta x_i\, \vec{e}_i) - \theta(\gamma)}{\Delta x_i},$$

where $\mathbf{x} = (x_1, x_2, \ldots, x_n)$ and $\vec{e}_i$ denotes the ith basis vector of $\mathbb{R}^n$. The direct method finds the partial derivatives $\frac{\partial}{\partial x_i}\theta(\gamma)$, $i = 1, 2, \ldots, n$, by comparing the phase of a base point

$\gamma \in \Gamma$ with the phases of solutions in the infinite-time limit, starting from points that are infinitesimally shifted from γ [4, 18, 46]. This method is straightforward and mimics how phase differences are measured in experiments.

The so-called adjoint method views $\nabla\theta(\gamma)$ as an eigenvector for the adjoint of the Jacobian matrix of the time-T_Γ map evaluated at γ. The classical derivation uses Taylor expansions of the orbit through an infinitesimal perturbation of γ; see [4, 16, 17, 27, 28] for more details. However, this approach is essentially the same as computing the linear stable normal bundle of Γ, which defines the linear approximation of $\mathcal{I}(\gamma)$, $\gamma \in \Gamma$. Let us explain this briefly because it is directly related to the method we use in this paper.

Consider the $n \times n$ Jacobian matrix of the time-T_Γ map $\Phi^{T_\Gamma}(\cdot)$ evaluated at γ. Since we assume that Γ is hyperbolic, this matrix $D\Phi^{T_\Gamma}(\gamma)$ has exactly one eigenvalue equal to 1— the associated eigenvector is the direction tangent to Γ at γ—and the other $n-1$ eigenvalues (counted with multiplicity) are all inside the complex unit circle; that is, they all have modulus less than 1. The $(n-1)$-dimensional hyperplane spanned by the (generalized) eigenvectors associated with these eigenvalues with modulus less than 1 is the linear approximation of $\mathcal{I}(\gamma)$. If $n = 2$, then the linear approximation of $\mathcal{I}(\gamma)$ is simply given by the eigenvector associated with the only stable eigenvalue of $D\Phi^{T_\Gamma}(\gamma)$. As soon as $n > 2$, however, it is more natural to define this linear approximation by a vector perpendicular to $\mathcal{I}(\gamma)$ at γ. Indeed, this perpendicular vector is precisely $\nabla\theta(\gamma)$, and it is given by the left eigenvector $\vec{\mathbf{v}}_\gamma$ associated with the trivial eigenvalue 1 of $D\Phi^{T_\Gamma}(\gamma)$. (Recall that a left eigenvector of a matrix is a right eigenvector of its adjoint.)

The standard method for finding $\vec{\mathbf{v}}_\gamma$ for any base point $\gamma \in \Gamma$ is the power method; the eigenvalue 1 is the largest eigenvalue of (the adjoint of) $D\Phi^{T_\Gamma}(\gamma)$, so an arbitrary vector direction converges to $\vec{\mathbf{v}}_\gamma$ when multiplied iteratively with this matrix. The Jacobian matrix $D\Phi^{T_\Gamma}(\gamma)$ is approximated using finite differencing, and the standard method uses backward integration along the periodic orbit Γ. For example, XPP [16] uses this method for finding PRCs numerically, and MATLAB code for this approach can be found in [28, Chapter 10].

2.2. Linear approximation as a two-point BVP. We propose a more direct method for computing $\vec{\mathbf{v}}_\gamma$ and the associated family for all $\gamma \in \Gamma$ that defines the linear stable normal bundle. The idea is to compute Γ and this associated vector bundle in a single two-point BVP; see [12, 13, 33] and, in particular, [9, 19], where this idea is used in the particular context of computing infinitesimal PRCs. We do not already assume knowledge of Γ. Instead, we combine (2.1) with the first variational equation

$$(2.3) \qquad \begin{cases} \dfrac{d\mathbf{x}}{dt} = F(\mathbf{x}), \\[2mm] \dfrac{d\vec{\mathbf{v}}}{dt} = \mathrm{adj}[DF(\mathbf{x})]\,\vec{\mathbf{v}}. \end{cases}$$

Here, $\mathrm{adj}[DF(\mathbf{x})]$ is the transpose (or adjoint) of the Jacobian matrix DF of the flow evaluated at a point $\mathbf{x}$ that varies in time according to the first equation of (2.3). Of course, this first equation should define the periodic orbit Γ, so we impose the boundary condition

$$(2.4) \qquad \mathbf{x}(T_\Gamma) = \mathbf{x}(0) =: \gamma,$$

where the period T_Γ of Γ is unknown. The first variational equation is the second equation of (2.3); it is linear, but with a time-varying matrix, and its solution is a vector bundle $\vec{\mathbf{v}} = \vec{\mathbf{v}}(t)$. As the initial condition, we require $\vec{\mathbf{v}}(0) = \vec{\mathbf{v}}_\gamma \in \mathbb{R}^n$. Note that (2.4) automatically implies that $DF(\mathbf{x})$, and thus its adjoint, is also periodic; if the linear bundle is orientable, this period is the (unknown) period T_Γ, and if it is nonorientable, we may set up the computation using period $2T_\Gamma$ for both Γ and its normal bundle. Consequently, the vector bundle $\vec{v}$ that is associated with an eigenvector of $D\Phi^{T_\Gamma}(\gamma)$ is periodic in the sense that the vector direction is mapped to itself after one full period, which we denote T_Γ for both orientable and nonorientable cases from now on. Indeed, the length of $\vec{\mathbf{v}}_\gamma$ shrinks or expands by a factor that is equal to the Floquet multiplier associated with this vector bundle. However, we are interested in the vector bundle associated with the trivial Floquet multiplier, so we have

$$\text{(2.5)} \qquad\qquad \vec{\mathbf{v}}(T_\Gamma) = \vec{\mathbf{v}}(0) =: \vec{\mathbf{v}}_\gamma,$$

and we assume that $\vec{\mathbf{v}}_\gamma$ is normalized to unit length. The combined system (2.3)–(2.5) is well posed and defines the solution up to a phase condition that fixes γ. Note that the trivial bundle $\vec{\mathbf{v}} \equiv 0$ for Γ is a solution that coexists with the actual eigenvector bundle we are after. Since the trivial bundle is a solution for any Floquet multiplier, one can find the nontrivial vector bundle as a branching solution from the trivial family that bifurcates at the particular Floquet multiplier 1; we refer to [12, 13, 33] for details.

We note here that for planar systems the vector bundle is always orientable. Furthermore, it is just as easy to compute the linear stable normal bundle $\vec{\mathbf{n}}^s$ directly by using

$$\text{(2.6)} \qquad\qquad \begin{cases} \dfrac{d\vec{\mathbf{n}}^s}{dt} &= DF(\mathbf{x})\,\vec{\mathbf{n}}^s, \\[2mm] \vec{\mathbf{n}}^s(T_\Gamma) = \mu^{T_\Gamma}\,\vec{\mathbf{n}}^s(0), \end{cases}$$

combined with (2.1) and (2.4). Here, μ is the stable Floquet multiplier of Γ. (Note that we use the Jacobian rather than its adjoint here.) Since μ can be extremely close to 0 in systems with multiple time scales, it can be advantageous to use a logarithmic formulation in terms of the Floquet exponent: When we set $\mu = e^\lambda$ and $\vec{\mathbf{n}}^s = e^{\lambda t}\,\vec{\mathbf{w}}$, the equation for the first variational part becomes

$$\begin{cases} \dfrac{d\vec{\mathbf{w}}}{dt} &= DF(\mathbf{x})\,\vec{\mathbf{w}} - \lambda\,\vec{\mathbf{w}}, \\[2mm] \vec{\mathbf{w}}(T_\Gamma) = \vec{\mathbf{w}}(0). \end{cases}$$

We again refer to [12, 13, 33] for details.

2.3. Higher-order local approximations of isochrons. We end with a brief discussion of higher-order methods. As mentioned, the first such method in the context of computing local approximations of isochrons was published only recently in [22]. However, any higher-order method for computing local stable manifolds can be adapted for this purpose. For example, Taylor expansions [41] are used to find higher-order approximations of local manifolds, and this technique has recently been studied in the context of higher-order approximations of the asymptotic phase function θ [43]; see also [24] for similar formulations of higher-order jets along manifolds, and [39] for a recursive implementation of the higher-order derivatives.

Guillamon and Huguet [22] use the so-called parameterization method that is originally designed for computing invariant manifolds [5]; that is, they view the isochron $\mathcal{I}(\gamma)$ as a leaf of the invariant foliation of the stable manifold of Γ at γ. The parameterization method uses Fourier expansions to represent the manifold. In principle, this approach results in high-order approximations that are valid in a relatively large neighborhood of Γ and lead to global approximations of the isochrons. However, it appears that Fourier expansions are not ideal for systems with multiple time scales, because the convergence of the expansion is typically slow and many terms are needed to obtain reasonably large portions of the isochrons; see [22] for details. Therefore, in [22] the parameterization method is used only for computing a local approximation of $\mathcal{I}(\gamma)$, which is then extended by other means to obtain a global approximation of the isochron.

3. Extending the isochrons. Globally, the isochrons are nonlinear (immersed) manifolds formed by the leaves of the invariant foliation of the stable manifold of the periodic orbit Γ [21, 25]. As mentioned before, the isochron $\mathcal{I}(\gamma)$ of a point $\gamma \in \Gamma$ is the stable manifold $W^{ss}(\gamma)$ that is invariant under the time-T_Γ map $\Phi^{T_\Gamma}(\cdot)$ and associated with the fixed point γ. The dynamics on $\mathcal{I}(\gamma)$ generated by $\Phi^{T_\Gamma}(\cdot)$ is a contraction; that is, $\mathcal{I}(\gamma)$ is an overflowing manifold and any local approximation can be extended by inverse iterations of $\Phi^{T_\Gamma}(\cdot)$. The methods described in sections 2.1–2.3 can be used to obtain a local approximation of $\mathcal{I}(\gamma)$ that is valid only in a small neighborhood of Γ. Throughout this section we focus on planar vector fields; that is, $\mathcal{I}(\gamma)$ is one-dimensional. Then we can employ standard techniques for the computation of global stable manifolds to compute global extensions of $\mathcal{I}(\gamma)$; see, for example, the discussion of such methods in [30].

To our knowledge, iterates of the inverse of $\Phi^{T_\Gamma}(\cdot)$ have, thus far, been computed only by numerical integration. The most straightforward way is to integrate the flow backward in time, but forward integration techniques using shooting have also been employed [6]. We specifically mention two recent publications that use backward integration methods, namely, by Sherwood and Guckenheimer [40] and by Guillamon and Huguet [22]. Unfortunately, biological oscillators often give rise to models with multiple time scales, which are rather sensitive to numerical integration. In such cases, the computation of large extensions of a local isochron with backward integration requires exponentially small variations in the initial condition, which cannot be achieved using standard double-precision arithmetic.

In the next section we propose a new method for computing global extensions of isochrons based on the continuation of BVPs [31]. Our approach is particularly well suited for systems with multiple time scales, because it does not rely on high-precision knowledge of initial conditions. The accuracy of the method uses information of the flow along entire orbit segments. Furthermore, the continuation automatically generates a mesh parameterized by arclength.

3.1. Global isochrons as a family of orbit segments. The method we propose for computing global extensions of isochrons is also based on the idea of viewing the isochron $\mathcal{I}(\gamma)$ of a point $\gamma \in \Gamma$ as a stable manifold $W^{ss}(\gamma)$ of $\Phi^{T_\Gamma}(\cdot)$. The set-up is very similar to that in [15] for the computation of one-dimensional manifolds of the fixed point of a Poincaré map that is associated with a periodic orbit of the underlying vector field. Indeed, the isochron of a point γ on Γ is nothing but the Poincaré section through γ of the time-T_Γ return map $\Phi^{T_\Gamma}(\cdot)$. In [15] the Poincaré section is known, and the associated Poincaré map is unknown

but defined implicitly as the (local) return to this section. In the present setting, the Poincaré map is defined as the time-T_Γ map, and the associated section is not known. If (2.1) were a periodically forced system with forcing period T_Γ, then the Poincaré section of the time-T_Γ map would be the phase space at fixed T_Γ-periodic time intervals. Hence, for this special case both the Poincaré map and the section are known explicitly. In general, however, the section associated with the time-T_Γ map is defined implicitly by the fact that points return to it after precisely the period T_Γ of Γ. This unknown Poincaré section is the isochron $\mathcal{I}(\gamma)$ that we wish to compute.

Just as for the integration methods mentioned above, we assume knowledge of a first local approximation of the isochron $\mathcal{I}(\gamma)$. We find that the linear approximation is sufficient for finding good global approximations of $\mathcal{I}(\gamma)$ [30, 35]. Particularly in the context of systems with multiple time scales, the contraction rates along the manifolds are extremely strong, which means that one can start with a local approximation in a very small neighborhood of Γ and still grow the manifold rapidly away from Γ. We compute the linear approximation of $\mathcal{I}(\gamma)$ with the method described in section 2.2. Let us assume that we have computed the vector direction $\vec{\mathbf{v}}_\gamma \in \mathbb{R}^2$ that is perpendicular to the linear approximation $\vec{\mathbf{n}}_\gamma^s \in \mathbb{R}^2$ of $\mathcal{I}(\gamma)$. We define the line segment

$$(3.1) \qquad\qquad L_\eta(\gamma) := \{\gamma + \delta\vec{\mathbf{n}}_\gamma^s \mid 0 \leq |\delta| \leq \eta\},$$

parameterized by δ. For $\eta \ll 1$ this line segment gives a good approximation of $\mathcal{I}(\gamma)$, and we denote points on it by $L_\eta(\gamma; \delta)$.

We view $\mathcal{I}(\gamma)$ as defined by a one-parameter solution family of a two-point BVP. Since we implemented our method in AUTO [11], we use AUTO notation to formulate the BVP. We consider orbit segments $\{\mathbf{u}(t) \mid 0 \leq t \leq 1\}$ that correspond to orbit segments $\{\mathbf{x}(t) \mid 0 \leq t \leq T_\Gamma\}$ of (2.1). That is, we consider orbit segments on the time interval $[0,1]$ of the rescaled vector field

$$(3.2) \qquad\qquad \dot{\mathbf{u}} = T_\Gamma \, F(\mathbf{u}).$$

An orbit segment corresponds to a point on $\mathcal{I}(\gamma)$ if both $\mathbf{u}(0)$ and $\mathbf{u}(1)$ are on $\mathcal{I}(\gamma)$. Note that the two points $\mathbf{u}(0)$ and $\mathbf{u}(1)$ are related, because we keep T_Γ fixed. The idea is now to find $\mathbf{u}(0)$ such that $\mathbf{u}(1)$ lies on the *numerical approximation* of $\mathcal{I}(\gamma)$. Initially, all we have is the linear approximation of $\mathcal{I}(\gamma)$, which leads to the boundary condition

$$(3.3) \qquad\qquad \mathbf{u}(1) = L_\eta(\gamma; \delta),$$

for some δ with $0 \leq |\delta| \leq \eta \ll 1$, where η is prespecified. The fact that we keep T_Γ fixed serves as a second condition, giving a unique solution for given δ. We can now solve the BVP (3.2)–(3.3) by continuation, where we keep T_Γ fixed and use δ as a free parameter. The periodic orbit Γ starting at γ solves (3.2)–(3.3) for $\delta = 0$. Hence, the continuation can be started from the known solution

$$(3.4) \qquad\qquad \mathbf{u}_\Gamma := \{\mathbf{u}(t) \mid 0 \leq t \leq 1, \, \mathbf{u}(0) = \mathbf{u}(1) = \gamma\}.$$

We use AUTO [11] for the continuation and let δ vary from 0 to η. Since AUTO [11] adapts the continuation step size automatically, we obtain a good distribution of points along the

isochron and can easily monitor the arclength of the approximation. The major advantage of this method over the integration methods mentioned earlier is the fact that AUTO [11] measures the variation between two orbit segments along the entire orbit segment and not just at the initial value. This avoids the extreme sensitivity on initial conditions that is so typical for multiple-time-scale systems. As a result, we are able to compute isochrons up to very long arclengths.

The continuation of the BVP (3.2)–(3.3) extends the isochron $\mathcal{I}(\gamma)$ from the linear approximation $L_\eta(\gamma)$ of arclength $2\eta \ll 1$ up to a longer nonlinear approximation that typically has an arclength of order $O(1)$ for multiple-time-scale systems. There are two different techniques for extending $\mathcal{I}(\gamma)$ further. In the spirit of [15], one can change the boundary condition (3.3) to restrict $\mathbf{u}(1)$ to the new longer approximation of $\mathcal{I}(\gamma)$. This works well as long as the curvature along $\mathcal{I}(\gamma)$ does not grow very large. For the example in section 4 we use a different technique: we perform continuation for the time-$(2T_\Gamma)$ map; that is, we compute the family of orbit segments that return to $L_\eta(\gamma)$ after two full periods T_Γ of Γ, then for the time-$(3T_\Gamma)$ map, and so on, as follows. Suppose that after the continuation for the time-$((k-1)T_\Gamma)$ map, we have $\delta = \eta$ and the corresponding solution is

$$\begin{aligned}\mathbf{u}_{\text{last}} &:= \{\mathbf{u}(t) \mid 0 \le t \le 1,\, \mathbf{u}(1) = L_\eta(\gamma; \eta)\} \\ &= \{\mathbf{x}(t) \mid 0 \le t \le (k-1)\,T_\Gamma,\, \mathbf{x}((k-1)\,T_\Gamma) = L_\eta(\gamma; \eta)\}.\end{aligned}$$

We then start a new continuation run, where we solve

$$\dot{\mathbf{u}} = kT_\Gamma\, F(\mathbf{u}),$$

with the same boundary condition (3.3) as before. The continuation can be started by concatenating the solutions $\mathbf{u}_{\text{last}}$ and $\mathbf{u}_\Gamma$ and rescaling them back to the $[0,1]$ interval. That is, we define

$$(3.5) \qquad \mathbf{u}(t) = \begin{cases} \mathbf{u}_{\text{last}}(k\,t), & 0 \le t \le \frac{k-1}{k}, \\ \mathbf{u}_\Gamma(k\,(t-1)+1), & \frac{k-1}{k} < t \le 1. \end{cases}$$

Of course, the concatenation contains a small discontinuity (or jump) at $t = \frac{k-1}{k}$, but as a seed solution for Newton's method, this will typically converge to a proper solution and successfully start the continuation. If the convergence fails because the discontinuity is too large, then more advanced techniques based on Lin's method can be employed; see [33] and references therein for details.

Our method is implemented in AUTO [11] using the Python interface, such that it automatically computes an arbitrary number of isochrons uniformly distributed in time or arclength along the periodic orbit up to a prespecified number of returns; the algorithm ISOCHRON for computing one isochron reads in pseudocode as follows.

ALGORITHM ISOCHRON.

Input: F,   right-hand-side of vector field stored in AUTO file `F.f`;

    Γ,   periodic orbit starting at $\gamma = \Phi^{\theta T_\Gamma}(\gamma_0)$ for some $\theta \in [0,1)$;

           stored in AUTO file `s.`Γ with parameters as follows:

    $\gamma \in \mathbb{R}^2$,   phase point on Γ and

$\vec{\mathbf{n}}_\gamma^s \in \mathbb{R}^2,$ normalized linear approximation of $\mathcal{I}(\gamma)$, define $L_\eta(\gamma)$,

$\delta \in \mathbb{R},$ distance along $\vec{\mathbf{n}}_\gamma^s$ is initially 0, can be accessed as $\mathsf{PAR}(25)$;

Global variables:

    $\eta,$ maximal distance on $\vec{\mathbf{n}}_\gamma^s$;

    $k,$ number of iterates of $\Phi^{T_\Gamma}(\cdot)$ to be considered;

Output: branch of global isochron $\mathcal{I}(\gamma)$ up to kth iterate of $\Phi^{T_\Gamma}(\cdot)$

         stored in AUTO file `b.iso` with each point stored as $(\mathsf{PAR}(26), \mathsf{PAR}(27))$;

Begin

δ = 0

\# Step 1: Continuation from Γ until distance δ along $\vec{\mathbf{n}}_\gamma^s$ reaches η

`run(equation='F', start='s.`Γ`', `δ`, `η`)`

\# last computed solution (where $\delta = \eta$) of first iterate is stored in file `s.last`

`save('s.last')`

\# computed branch forms first part of global isochron $\mathcal{I}(\gamma)$

`save('b.iso')`

\# Step 2: Restart with second and higher iterates

`for i in range(2, `k`)`

    \# Append Γ in `s.`Γ to last computed solution in `s.last` to continue

    `s.concat = `CONCATENATE`(s.last, s.`Γ`)`

    \# Increase the number of mesh intervals accordingly

    $\mathsf{NTST} = \mathsf{NTST}_{\text{last}} + \mathsf{NTST}_\Gamma$

    δ = 0

    `run(equation='F', start='s.concat', `δ`, `η`)`

    \# last computed solution (where $\delta = \eta$) of ith iterate is stored in file `s.last`

    `save('s.last')`

    \# computed branch forms extension of global isochron $\mathcal{I}(\gamma)$

    `append('b.iso')`

End.

The procedure CONCATENATE in ISOCHRON performs the concatenation (3.5). The continuation uses an AUTO constant file as given in Table 1, which is the constants file for the example of the reduced Hodgkin–Huxley model in section 4. Here, standard AUTO notation is used for the constants. In particular, NTST and NCOL specify the number of mesh intervals

Table 1

Accuracy parameters in the AUTO [11] constants file as used in the example of the reduced Hodgkin–Huxley system in section 4. Note that the number of mesh intervals NTST increases with each iteration of the return map $\Phi^{\Gamma_T}(\cdot)$. We refer to the AUTO manual [11] for further details on the meaning of these parameters.

$\mathsf{NDIM} = 3,$	$\mathsf{IPS} = 4,$	$\mathsf{IRS} = 0,$	$\mathsf{ILP} = 0$				
$\mathsf{ICP} = [\mathsf{PAR}(25), \mathsf{PAR}(26), \mathsf{PAR}(27)]$							
$\mathsf{NTST} = 100,$	$\mathsf{NCOL} = 4,$	$\mathsf{IAD} = 3,$	$\mathsf{ISP} = 0,$	$\mathsf{ISW} = 1,$	$\mathsf{IPLT} = 0,$	$\mathsf{NBC} = 4,$	$\mathsf{NINT} = 0$
$\mathsf{NMX} = 5000,$	$\mathsf{NPR} = 1,$	$\mathsf{MXBF} = 0,$	$\mathsf{IID} = 2,$	$\mathsf{ITMX} = 8,$	$\mathsf{ITNW} = 5,$	$\mathsf{NWTN} = 3,$	$\mathsf{JAC} = 0$
$\mathsf{EPSL} = 10^{-8},$		$\mathsf{EPSU} = 10^{-8},$		$\mathsf{EPSS} = 10^{-6}$			
$\mathsf{DS} = 10^{-5} = 0.1\,\eta,$		$\mathsf{DSMIN} = 10^{-8},$		$\mathsf{DSMAX} = 10^2,$		$\mathsf{IADS} = 1$	
$\mathsf{THL} = \{\mathsf{PAR}(11) : 0.0\},$		$\mathsf{UZR} = \{\mathsf{PAR}(25) : [-\eta, \eta]\},$				$\mathsf{STOP} = [\text{'UZ1'}]$	

and collocation points used in AUTO to compute the periodic orbit Γ. Initially, NTST equals the number NTST_Γ of mesh intervals used for the computation of Γ. The kth iterate of $\Phi^{\Gamma_T}(\cdot)$ uses $\mathsf{NTST} = k \times \mathsf{NTST}$ mesh intervals, due to the concatenation of the end solution $\mathbf{u}_{\text{last}}$ of the $(k-1)$st iterate with the solution $\mathbf{u}_\Gamma$ of the periodic orbit. The solution of the BVP is computed with a Newton/Chord method using a maximum of ITNW iterates, where the Jacobian matrix is kept fixed after NWTN iterates. The convergence criterion is EPSL for the parameters and EPSU for the solution components; the stop criterion $|\delta| = \eta$ is determined with accuracy EPSS using a maximum of ITMX iterates. The continuation starts with a step size DS, which should be less than η.

3.2. Computational accuracy. While a complete error analysis of our method is beyond the scope of this paper, we include here a brief discussion of the accuracy of the computations. The computational error arises from two sources: the fact that we start on the linear approximation of the isochron and the fact that iterates of the map $\Phi^{T_\Gamma}(\cdot)$ must be calculated numerically. These two errors can be analyzed separately, and the combined influence is typically measured assuming that the numerical integration error is negligible compared to the error from starting on the linear approximation. However, particularly in systems with multiple time scales, this underlying assumption can easily be violated.

We calculate iterates of $\Phi^{T_\Gamma}(\cdot)$ by solving BVPs with the method of orthogonal collocation with piecewise polynomials, as implemented in AUTO [11]. The order of accuracy of the orthogonal collocation method is NCOL with superconvergence at the end points of the mesh intervals and the parameters [3, 10]. If we assume that the discretization used to obtain $\Phi^{T_\Gamma}(\cdot)$ is sufficiently accurate, then the accuracy of the isochrons is fully controlled by the maximal distance η on the linear approximation. Note that the computation of isochrons is the same as computing a stable manifold; hence the same error analysis applies. However, the associated fixed point, that is, the phase point $\gamma \in \Gamma$ for which the isochron is computed, is not an isolated fixed point of $\Phi^{T_\Gamma}(\cdot)$. Hence, γ is not hyperbolic, and we must adapt the error analysis given in [30] for manifolds of hyperbolic fixed points; specifically, we must take into account that the local contraction rates on the manifold are algebraic, rather than exponential, and follow the analysis in [35] for manifolds of nonhyperbolic equilibria of vector fields.

In practice, it is very difficult to estimate the computational error a priori as well as a posteriori. For example, we have no explicit error bounds for the computations of isochrons for the reduced Hodgkin–Huxley model in the next section. However, the numerical computations show a consistency that is maintained (at least) up to the arclengths of our computations: the numerically computed isochrons do not intersect themselves or each other, even if a very large number are computed to show the foliation of the plane. We believe that this consistency is a powerful argument that the resulting structure of the isochrons is correct; see [30] for an example where this argument is used to illustrate the contrary, because the structure that results from computing the invariant manifolds violates the theory.

4. Isochrons of the reduced Hodgkin–Huxley model. To illustrate the method for computing isochrons, we consider a two-dimensional reduced model of the Hodgkin–Huxley equations [26]. The model is based on the dynamical interplay between ionic conductances and electrical activity using the voltage, V, and three gating variables, denoted m, n, and h, for the conductance channels. In the reduced planar model the gating variable m is replaced by

its quasi–steady-state function $m_\infty(V)$, and the gating variable h is replaced by $0.8 - n$, which is a reasonable approximation of its average value; see [28, 29, 34]. The reduced model of the Hodgkin–Huxley equations can then be written as the vector field

(4.1)
$$\begin{cases} \dot{V} = \dfrac{1}{C} \left[I_{\text{app}} - \bar{g}_{Na} \left[m_\infty(V) \right]^3 (0.8 - n)(V - V_{Na}) \right. \\ \left. \qquad - \bar{g}_K\, n^4\,(V - V_K) - g_L(V - V_L) \right], \\ \dot{n} = \alpha_n(V)\,(1 - n) - \beta_n(V)\,n, \end{cases}$$

where

$$\alpha_n(V) = \frac{0.01(V + 55)}{1 - \exp[-(V + 55)/10]}, \qquad \beta_n(V) = 0.125 \exp\left(\frac{-(V + 65)}{80} \right),$$

$$\alpha_m(V) = \frac{0.1(V + 40)}{1 - \exp[-(V + 40)/10]}, \qquad \beta_m(V) = 4 \exp\left(\frac{-(V + 65)}{18} \right),$$

$$m_\infty(V) = \frac{\alpha_m(V)}{\alpha_m(V) + \beta_m(V)},$$

and the parameters are given by

$$\begin{array}{llll} \bar{g}_{Na} = 120, & \bar{g}_K = 36, & g_L = 0.3, & I_{\text{app}} = 10, \\ V_{Na} = 50, & V_K = -77, & V_L = -54.4, & C = 1. \end{array}$$

System (4.1) has a stable periodic orbit Γ with period $T_\Gamma \approx 11.8463$; it is shown in Figure 1. Panel (a) gives the time series of Γ for the V-coordinate. The time series illustrates that Γ is a relaxation oscillation organized by the much slower dynamics of n relative to the dynamics of V. Panel (b) shows Γ in (V, n)-space along with the nullclines $\dot{V} = 0$ and $\dot{n} = 0$ in green and red, respectively. The nullclines intersect approximately at $\mathbf{x}^* := (V, n) \approx (-59.6044, 0.4026)$, which is the only equilibrium of (4.1). This equilibrium is a source with complex eigenvalues.

The slow-fast nature of (4.1) also has an effect on the location of the isochrons. Figure 2 shows the isochrons of one hundred points $\gamma_i = \Phi^{\theta_i T_\Gamma}(\gamma_0) \in \Gamma$ with phases $\theta_i = \frac{i}{100}$, for $i = 0, 1, \ldots, 99$. The isochrons are colored with a cyan-to-magenta color gradient with respect to their phases θ_i. Here, we associate the zero phase (cyan) with the point $\gamma_0 := (V, n) \approx (44.7064, 0.4597)$ on Γ where V is maximal; note that γ_0 must then lie on the V-nullcline. As can be seen in Figure 2, most isochrons start at points on Γ that are located close to the left branch of the V-nullcline (Γ intersects the left branch of the V-nullcline at only one point); this means that the phase changes most rapidly with respect to arclength along this segment of Γ. The density of isochrons in this region also nicely illustrates the fact that the foliation of isochrons indeed covers the entire phase plane.

Each isochron in Figure 2 has two branches, one on the outside of Γ and one on the inside. The branches on the outside of Γ go off to infinity with asymptotes that are almost horizontal. Indeed, the dynamics of points outside and far away from Γ is dominated by the V-velocity, and their asymptotic phases are mostly determined by their n-coordinates. Since the isochrons foliate the entire basin of attraction of Γ, which is the plane minus the equilibrium $\mathbf{x}^*$, the branches of the isochrons inside Γ must end up at $\mathbf{x}^*$, which is the phaseless set of (4.1).
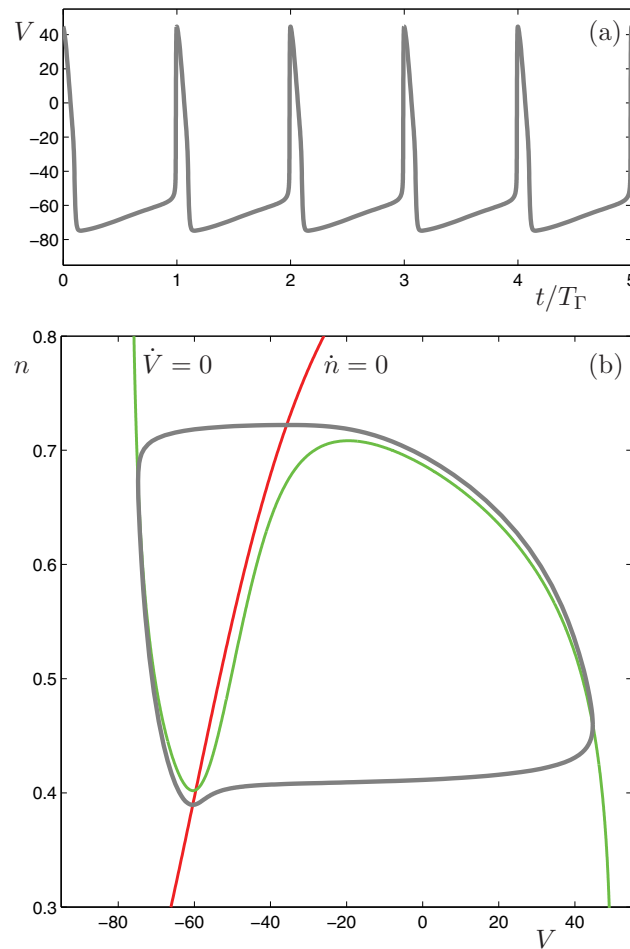
Figure 1. *The stable periodic orbit Γ (gray) of the reduced Hodgkin–Huxley model* (4.1). *Panel* (a) *shows the time series of the V-coordinate of Γ, which emphasizes the slow-fast nature of the model; panel* (b) *shows Γ in phase space along with the V-nullcline (green) and the n-nullcline (red) that intersect at the source equilibrium* $\mathbf{x}^*$ *(not labeled).*

However, Figure 2 seems to show isochrons that bend away from $\mathbf{x}^*$, and the accumulation onto $\mathbf{x}^*$ is not at all obvious. In the next section we focus on the specific behavior of a single isochron to investigate this seeming contradiction.

4.1. The 0-phase isochron. The isochron branches inside Γ do end up at the equilibrium $\mathbf{x}^*$, but the accumulation process is rather complicated. Figure 3 shows the 0-phase isochron of Γ, that is, for the point γ_0 with maximal V that lies on the intersection of Γ with the V-nullcline. We colored $\mathcal{I}(\gamma_0)$ such that its color changes from red to blue as the arclength distance to γ_0 increases. The linear approximation of the isochron is almost horizontal here, and we found $\vec{v}_{\gamma_0} := (0.99999988, -0.00013711)$. Figure 3(a) shows the isochron $\mathcal{I}(\gamma_0)$ computed up to the time-$(4T_\Gamma)$ map for a maximum distance of $\delta = \eta = 10^{-4}$ on the linear approximation. By moving a point along $\mathcal{I}(\gamma_0)$ starting at γ_0, we illustrate with the accompanying animation (77724_01.gif [393KB]) how the inside branch approaches $\mathbf{x}^*$. The
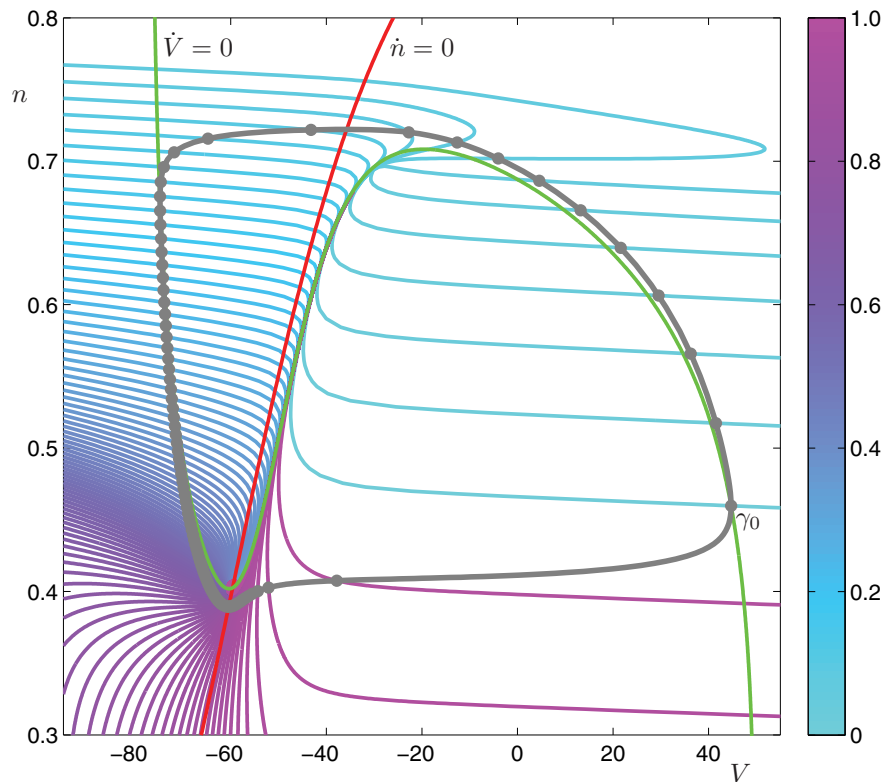
Figure 2. *A total of* 100 *isochrons uniformly distributed in time along the stable periodic orbit (gray) of the reduced Hodgkin–Huxley model* (4.1)*, colored according to their phases. The* 0*-phase point* γ_0 *is labeled, and the V-nullcline (green) and the n-nullcline (red) are included for reference.*

equilibrium $\mathbf{x}^*$ is not labeled in the figure, but it lies at the intersection of the two nullclines. In panel (b), the n-coordinate along $\mathcal{I}(\gamma_0)$ is plotted versus its arclength, where the arclength is 0 at γ_0. We see that $\mathcal{I}(\gamma_0)$ initially stays almost horizontal (it is roughly linear) until it comes close to the V-nullcline. Then, instead of approaching $\mathbf{x}^*$ directly, $\mathcal{I}(\gamma_0)$ bends around and moves away from $\mathbf{x}^*$ while it closely follows the V-nullcline. At some maximum value $n \approx 0.6802$, where the arclength of $\mathcal{I}(\gamma_0)$ is a little over 100, the isochron bends back virtually on top of itself toward $\mathbf{x}^*$. We call this behavior of the isochron an "excursion." After this first excursion, $\mathcal{I}(\gamma_0)$ makes a counterclockwise loop around $\mathbf{x}^*$ before moving back up along the V-nullcline. During this second excursion, $\mathcal{I}(\gamma_0)$ does not come as high as during the first, reaching $n \approx 0.5517$. On the way down, $\mathcal{I}(\gamma_0)$ first makes a clockwise loop around $\mathbf{x}^*$ before turning around, making a counterclockwise loop, and moving back up for the third excursion. Figure 3(c) shows an enlargement near $\mathbf{x}^*$, where we can see the switches to counterclockwise loops as relatively sharp turns, which we call "boomerang turns." The continuation up to the time-($4T_\Gamma$) map gives three excursions and three boomerang turns, which form a spiral pattern that converges to $\mathbf{x}^*$. We find more excursions that involve an increasingly larger number of clockwise loops before a boomerang turn if we perform continuation for the time-(kT_Γ) map with $k > 4$. Panel (d) shows the value of $\dot{V}$ versus the arclength of $\mathcal{I}(\gamma_0)$ to illustrate that
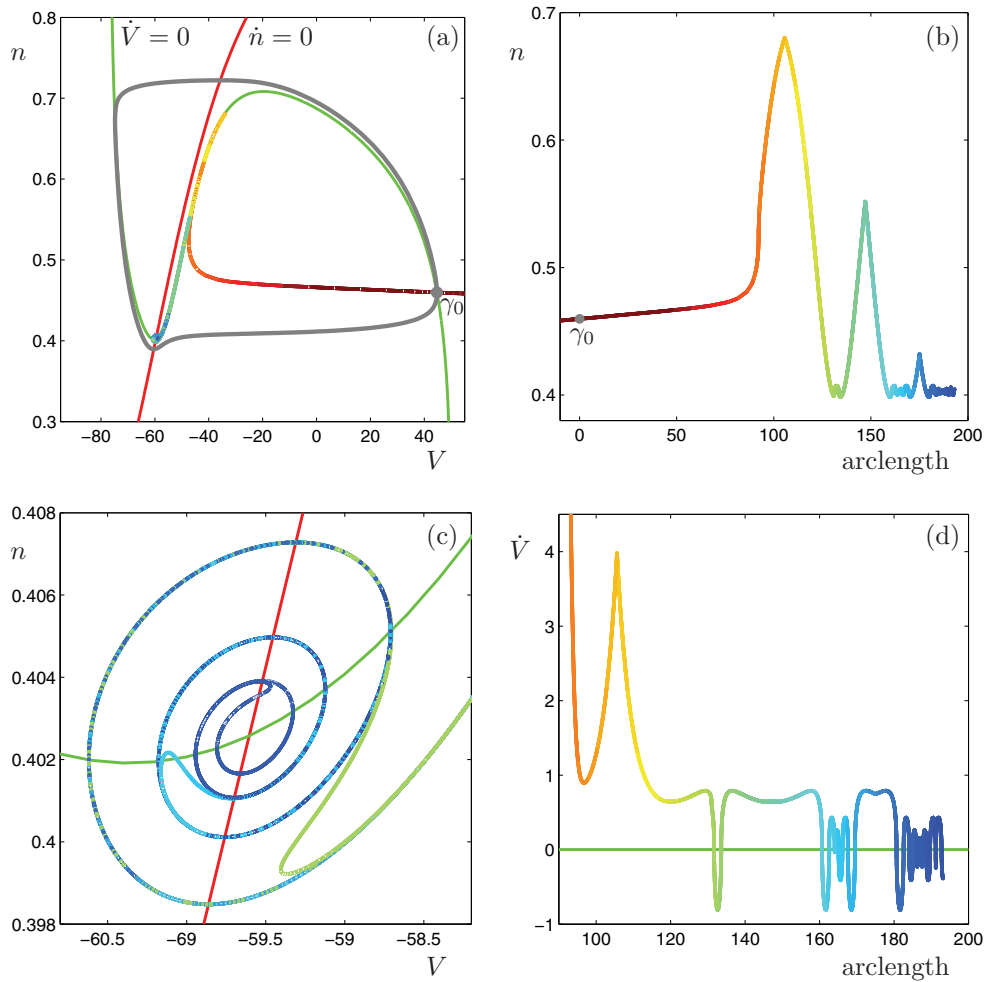
Figure 3. *The 0-phase isochron $\mathcal{I}(\gamma_0)$ of the point γ_0 on the stable periodic orbit (gray) of the reduced Hodgkin–Huxley model* (4.1) *is colored with a red-to-blue color gradient with respect to arclength distance to γ_0. Panel* (a) *shows $\mathcal{I}(\gamma_0)$ in the phase plane, where the V-nullcline (green) and the n-nullcline (red) are included for reference; panel* (b) *shows the n-coordinate of $\mathcal{I}(\gamma_0)$ versus its arclength—this panel also serves as a colorbar for the figure; panel* (c) *is an enlargement to illustrate the accumulation onto the equilibrium $\mathbf{x}^*$ (not labeled); panel* (d) *shows the value of $\dot{V}$ along $\mathcal{I}(\gamma_0)$ versus its arclength, where $\dot{V} > 0$ below the V-nullcline (green) in panel* (c) *and $\dot{V} < 0$ above it. The associated animation (*77724_01.gif *[393KB]) shows a point moving along the inside branch of $\mathcal{I}(\gamma_0)$.*

$\mathcal{I}(\gamma_0)$ does not actually lie on the V-nullcline; the V-nullcline is the horizontal 0-axis (green) in Figure 3(d). In fact, $\mathcal{I}(\gamma_0)$ intersects the V-nullcline only when it loops around $\mathbf{x}^*$.

4.2. Global properties of the 0-phase isochron. The fact that we are able to compute very large portions of the isochron $\mathcal{I}(\gamma_0)$ as a one-dimensional curve parameterized by arclength allows us to study its properties in unprecedented detail. The excursions of $\mathcal{I}(\gamma_0)$ create curve segments that are extremely close to each other. By definition, each point on these curve segments arrives under the flow on the linear approximation $L_\eta(\gamma_0)$ with $\eta = 10^{-4}$
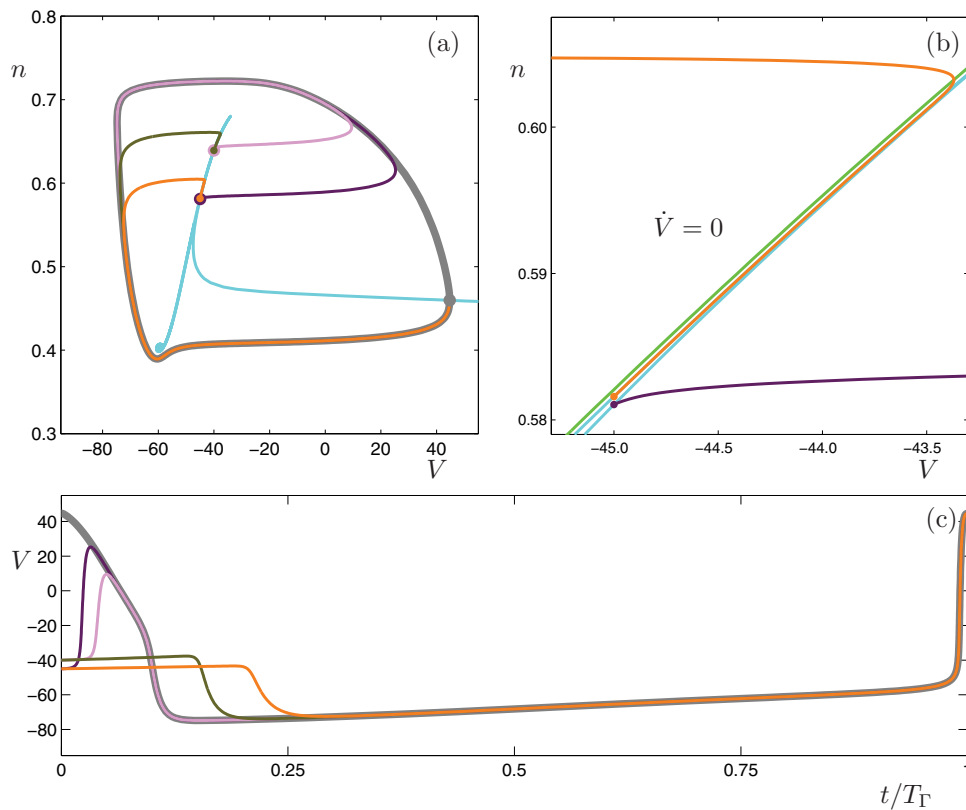
Figure 4. *Pairs of jump-right and jump-left orbits at $V = -45.0$ and $V = -40.0$ on the 0-phase isochron (cyan) of the reduced Hodgkin–Huxley model (4.1). All four orbit segments lie on $L_\eta(\gamma_0)$ with $\eta = 10^{-4}$ after one period. Panel (a) shows the phase plane; panel (b) is an enlargement illustrating that a jump-left orbit lies to the right of the V-nullcline (green); panel (c) shows the time series of V for these four orbit segments over one period, overlaid on the corresponding time series for the periodic orbit (gray). The associated animations (77724_02.gif [289KB] and 77724_03.gif [174KB]) show the in-phase convergence of a jump-right orbit at $V = -40.0$ and a jump-left orbit at $V = -45.0$, respectively.*

at *exactly the same time* modulo the period T_Γ. Hence, each point identifies a unique orbit segment in the one-parameter family of orbit segments that solves the BVP (3.2)–(3.3). Figure 4 shows four such orbit segments associated with four points along $\mathcal{I}(\gamma_0)$; they form two pairs, one with $V = -45.0$ and one with $V = -40.0$, that lie on corresponding pairs of segments of the first excursion. The isochron $\mathcal{I}(\gamma_0)$ has the same color as in Figure 2, namely, cyan. The phase portrait in panel (a) illustrates that one of the orbit segments in each pair suddenly moves to the left as it converges to Γ, while the other moves to the right; we call them jump-left and jump-right orbits, respectively. This does not necessarily mean that their initial conditions must lie on opposite sides of the V-nullcline, as is illustrated in Figure 4(b) for the pair with $V = -45.0$. Indeed, the jump-left orbit closely follows the V-nullcline and moves to the right until it crosses the V-nullcline before making the jump. Figure 4(c) shows the time series of the orbit segments; here, the jump-right orbits move up and the jump-left orbits move down before converging to Γ. These moves are indeed very fast in time, which is

why we refer to them as jumps. The initial plateaus in panel (c), particularly of the jump-left orbits, illustrate how the orbit segments linger close to the repelling branch of the V-nullcline in order to jump at exactly the right moment to meet $L_\eta(\gamma_0)$ after period T_Γ; see also the animations 77724_02.gif [289KB] and 77724_03.gif [174KB].

Figure 4(b) shows that pairs of jump-right and jump-left orbits that start with the same V-coordinate do not straddle the repelling branch of the V-nullcline. However, they must straddle the corresponding repelling slow manifold. A repelling slow manifold S_ε^r consists of all points with forward trajectories that stay $O(\varepsilon)$ close to the repelling branch of the critical manifold for $O(1)$ time, delimited by folds with respect to the fast flow; here, $0 < \varepsilon \ll 1$ represents the (local) ratio between the slow and fast time scales. For the reduced Hodgkin–Huxley model (4.1) the critical manifold is the one-dimensional V-nullcline, with the repelling branch in between its local maximum and minimum. We refer to [2, 8, 14] for more details on slow manifolds and their effects on the dynamics of the system. Since a slow manifold has the same dimension as the corresponding critical manifold, (4.1) has a one-dimensional repelling slow manifold S_ε^r that consists of a single orbit segment very close to the repelling branch of the V-nullcline. Hence, S_ε^r is an orbit segment, and neither jump-left nor jump-right orbits can cross it. The 0-phase isochron $\mathcal{I}(\gamma_0)$ winds around S_ε^r, with jump-left orbits starting from points on $\mathcal{I}(\gamma_0)$ that lie to the left of S_ε^r and jump-right orbits starting from points on $\mathcal{I}(\gamma_0)$ that lie to the right of it. Note that the points that correspond to jump-left orbits must lie closer to S_ε^r than those that correspond to jump-right orbits, because they linger near the V-nullcline for longer.

The second excursion of $\mathcal{I}(\gamma_0)$ consists of two segments that lie even closer to S_ε^r. Points on these segments correspond to orbit segments that reach $L_\eta(\gamma_0)$ after two periods T_Γ. This is illustrated in Figure 5. Panels (a) and (b) show phase portraits of two pairs of jump-right and jump-left orbits at $V = -55.0$ and $V = -50.0$, respectively. These orbits must follow S_ε^r for a relatively longer time, so that they reach $L_\eta(\gamma_0)$ only after the second full period; see their time series shown in panel (c). As in Figure 4(c), the jump-left orbits have the longest plateaus in Figure 5(c), and the jump-right orbits almost reach $L_\eta(\gamma_0)$ already during the first period.

The change from jump-right to jump-left orbits is continuous, by which we mean that the segments on $\mathcal{I}(\gamma_0)$ that correspond to jump-right and jump-left orbits are separated by short segments along which the concept of a left or right jump is not well defined. Indeed, close to the maximum of an excursion, $\mathcal{I}(\gamma_0)$ intersects S_ε^r. The repelling slow manifold S_ε^r is really a segment of an orbit $\mathbf{x}^r = \mathbf{x}^r(t)$ that converges to Γ. While it is not clear where $\mathbf{x}^r$ ceases to correspond to S_ε^r, the points on $\mathcal{I}(\gamma_0)$ near its intersection with S_ε^r correspond to orbits that closely follow $\mathbf{x}^r$, and they do not really "jump."

As $\mathcal{I}(\gamma_0)$ loops around $\mathbf{x}^*$, there is no nearby repelling slow manifold, although the orbit $\mathbf{x}^r$ that corresponds to S_ε^r continues all the way backward in time to $\mathbf{x}^*$. The points on segments of $\mathcal{I}(\gamma_0)$ near $\mathbf{x}^*$ also correspond to orbit segments that cannot easily be distinguished as jump-right or jump-left orbits. Figure 6 illustrates the behavior of the orbits generated from points on a part of $\mathcal{I}(\gamma_0)$ that loops around $\mathbf{x}^*$. We picked four orbit segments that all start on $\mathcal{I}(\gamma_0)$ with $V = -59.2$ and end on $L_\eta(\gamma_0)$ with $\eta = 10^{-4}$ after two periods T_Γ; the orbit segments are colored purple, pink, khaki green, and orange in the order of their initial conditions on $\mathcal{I}(\gamma_0)$. The orbit segments are shown in Figure 6(a), with an enlargement near $\mathbf{x}^*$ in panel (b)
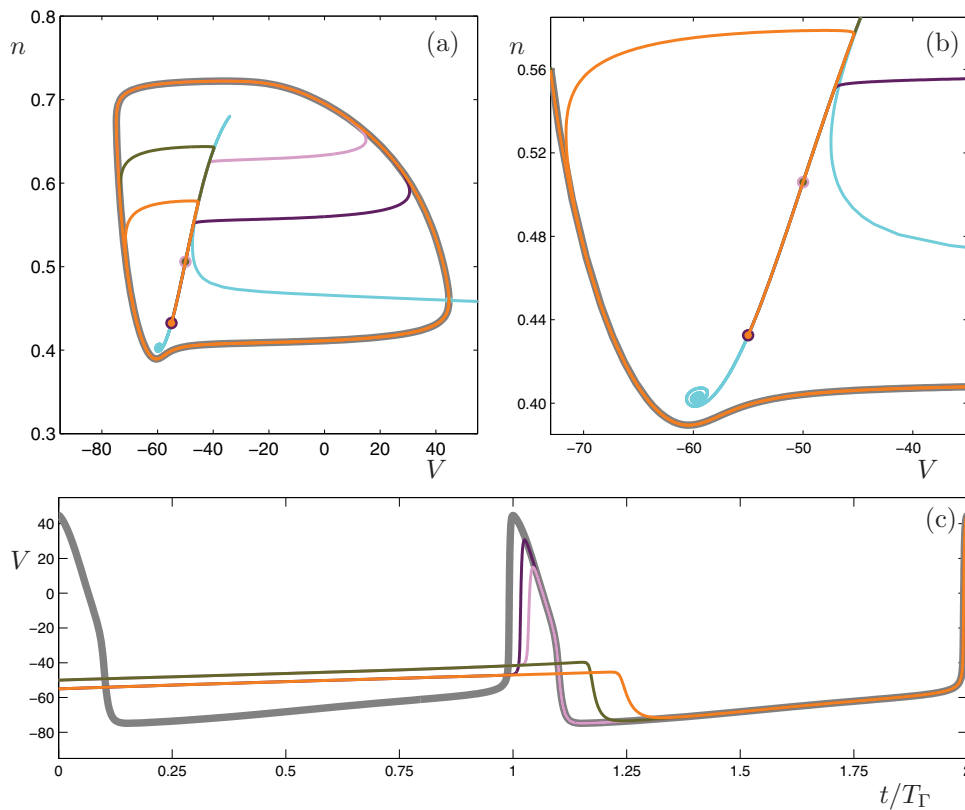
Figure 5. *Pairs of jump-right and jump-left orbits at $V = -55.0$ and $V = -50.0$ on the 0-phase isochron (cyan) of the reduced Hodgkin–Huxley model (4.1). All four orbit segments lie on $L_\eta(\gamma_0)$ with $\eta = 10^{-4}$ after two periods. Panel (a) shows the phase plane, with an enlargement in panel (b); panel (c) shows the time series of V for these four orbit segments over two periods, overlaid on corresponding time series for the periodic orbit (gray). The associated animations (77724_04.gif [357KB] and 77724_05.gif [354KB]) show the in-phase convergence of a jump-right orbit at $V = -55.0$ and a jump-left orbit at $V = -50.0$, respectively.*

and their time series in panel (c). Particularly in Figure 6(c), it is hard to decide whether the orbit segments actually jump. Their initial conditions are shown in Figure 6(b); note that even in this enlargement the first (purple) and last (orange) of these points lie virtually on top of each other. Following $\mathcal{I}(\gamma_0)$ down from the top-right in Figure 6(b) (which is covered by orange from the last orbit), the first (purple) orbit starts at the end of the first excursion just before $\mathcal{I}(\gamma_0)$ makes a counterclockwise loop around $\mathbf{x}^*$; this segment of the first excursion corresponds to jump-left orbits. The purple orbit does turn to the left, but it makes only a small loop around $\mathbf{x}^*$ before moving to the right instead. Similarly, the second (pink) orbit starts immediately after the first boomerang turn of $\mathcal{I}(\gamma_0)$ and makes a left turn in the sense that it loops around $\mathbf{x}^*$ before moving right. The third (khaki green) orbit segment starts into the counterclockwise loop and traces $\mathcal{I}(\gamma_0)$ back for a while before making a right jump; see Figure 6(a). One could say that this (khaki green) orbit closely follows the orbit $\mathbf{x}^r$, and, in fact, apart from the boomerang turns, there is a clear spiraling curve on $\mathcal{I}(\gamma_0)$ that seems to trace $\mathbf{x}^r$. Indeed, part of the last (orange) orbit segment lies almost on top of the khaki green
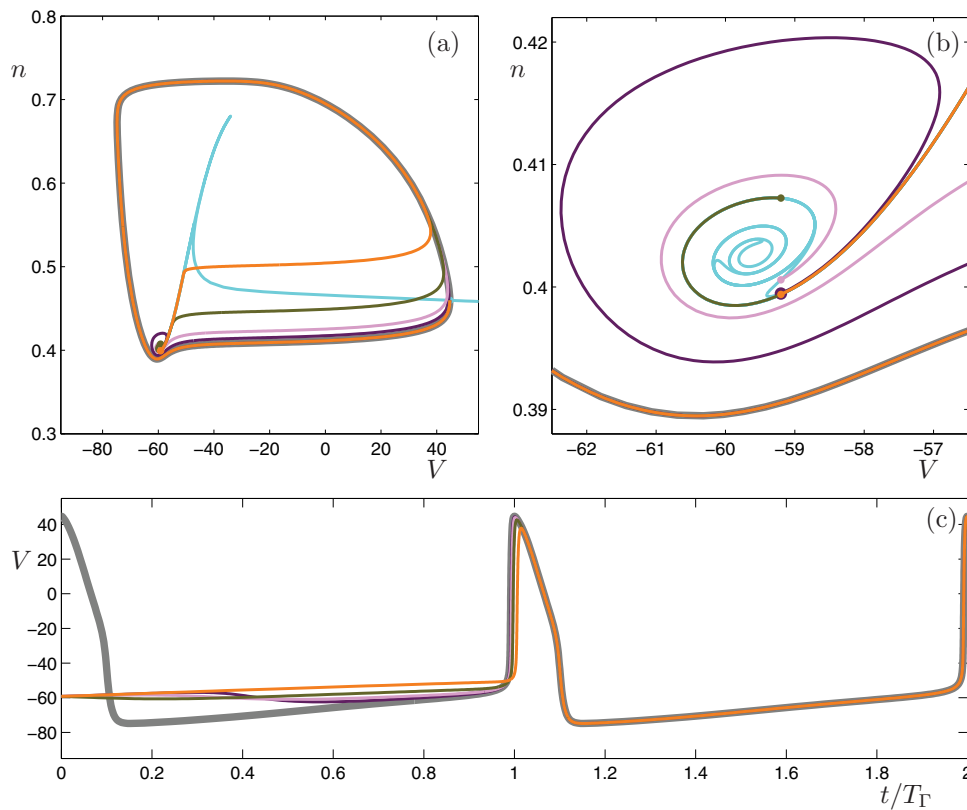
Figure 6. *The transition from jump-left to jump-right orbits as the 0-phase isochron (cyan) of the reduced Hodgkin–Huxley model (4.1) loops around the equilibrium. Four orbit segments are shown, each with $V = -59.2$. All four orbit segments lie on $L_\eta(\gamma_0)$ with $\eta = 10^{-4}$ after two periods. Panel (a) shows the phase plane, with an enlargement in panel (b); panel (c) shows the time series of V for these four orbit segments over two periods, overlaid on the corresponding time series for the periodic orbit (gray).*

orbit segment, but its starting point lies only past the loop around $\mathbf{x}^*$. This orbit segment has the distinct features of a jump-right orbit, marking the start of the second excursion.

The second excursion of $\mathcal{I}(\gamma_0)$ must necessarily intersect the repelling slow manifold S_ε^r, or more precisely, $\mathbf{x}^r$, at a point that lies exactly one period T_Γ earlier on $\mathbf{x}^r$ than the intersection point of the first excursion of $\mathcal{I}(\gamma_0)$ with $\mathbf{x}^r$. We can deduce from Figure 6 that the transition from the second excursion to the third excursion of $\mathcal{I}(\gamma_0)$ will happen in much the same way as the transition illustrated in Figure 6 for the first excursion. Note that the second boomerang turn on $\mathcal{I}(\gamma_0)$, shown in Figure 6(b), is a rotated and contracted version of the first boomerang turn; similar transitions with similar further rotated and contracted boomerang turns happen for all subsequent excursions; see also Figure 3(c), where the first three boomerang turns of $\mathcal{I}(\gamma_0)$ are colored pale green, light blue, and dark blue, successively.

4.3. Properties of all global isochrons. The previous two sections described the behavior of the single isochron for the point γ_0 with zero phase. Any other point γ on the periodic orbit Γ of the reduced Hodgkin–Huxley model (4.1) will have a different isochron associated with a different phase $\theta(\gamma)$. However, recall from (2.2) that the isochrons are diffeomorphic

transformations of $\mathcal{I}(\gamma_0)$; namely, this means that they are foliations of the stable manifold of Γ. Indeed, if $\gamma = \Phi^{\theta T_\Gamma}(\gamma_0)$, then

$$\mathcal{I}(\Phi^{\theta T_\Gamma}(\gamma_0)) = \Phi^{\theta T_\Gamma}(\mathcal{I}(\gamma_0)).$$

In other words, $\mathcal{I}(\gamma)$ can be obtained by integrating each point on $\mathcal{I}(\gamma_0)$ for the fixed time θT_Γ, where $\theta = \theta(\gamma)$ is the phase of γ. Note that forward integration leads to a contraction toward Γ. Since $\mathcal{I}(\gamma_0)$ is computed up to a finite arclength, the transformation of $\mathcal{I}(\gamma_0)$ under the flow $\Phi^{\theta T_\Gamma}$ will lead to an approximation of $\mathcal{I}(\gamma)$ that has a shorter arclength. For θ close to 1, the shortening is $O(1)$ due to the large difference in time scales of the system.

We compute all isochrons $\mathcal{I}(\gamma)$ in the same way as for $\mathcal{I}(\gamma_0)$; that is, we compute the stable manifold $W^{ss}(\gamma)$ as the invariant manifold of the time-T_Γ map that intersects the point γ on Γ. This means that the accuracy of $\mathcal{I}(\gamma)$ is the same as that of $\mathcal{I}(\gamma_0)$, and, in particular, we start with the linear approximation $L_\eta(\gamma)$ at γ using the same bound $\eta = 10^{-4}$. Figure 7 shows an example of the isochron $\mathcal{I}(\gamma_{30})$ with $\gamma_{30} = \Phi^{\theta_{30} T_\Gamma}(\gamma_0)$, where $\theta_{30} = \frac{30}{100} = 0.3$; this means that $\gamma_{30} := (V, n) \approx (-72.7092, 0.5480)$, and the direction tangent to $\mathcal{I}(\gamma_{30})$ is approximately given by the vector $\vec{v}_{\gamma_{30}} := (-0.99999972, 0.00075031)$. As for $\mathcal{I}(\gamma_0)$, we perform continuation up to the time-$(4T_\Gamma)$ map and color $\mathcal{I}(\gamma_{30})$ such that its color changes from red to blue as the arclength distance to γ_{30} increases. The figure is organized in the same way as Figure 3. Panel (a) shows $\mathcal{I}(\gamma_{30})$ in (V, n)-space along with the nullclines $\dot{V} = 0$ (green) and $\dot{n} = 0$ (red). The accompanying animation (77724_06.gif [221KB]) illustrates how the inside branch of $\mathcal{I}(\gamma_{30})$ approaches the equilibrium $\mathbf{x}^*$ at the intersection of the two nullclines; see also the enlargement in panel (c). Figure 7(b) shows the n-coordinate of $\mathcal{I}(\gamma_{30})$ versus its arclength. The isochron first moves toward $\mathbf{x}^*$, but then it makes a counterclockwise loop around $\mathbf{x}^*$ and starts making excursions, similar to those of $\mathcal{I}(\gamma_0)$, that closely follow the V-nullcline, or more precisely, the slow manifold S_ε^r that lies very close to the V-nullcline. The first two excursions are clearly seen in Figure 7(b); the first peak reaches $n \approx 0.5860$, which lies between the peaks from the first ($n \approx 0.6802$) and second ($n \approx 0.5517$) excursions of $\mathcal{I}(\gamma_0)$, and the second peak reaches $n \approx 0.4669$. In Figure 7(c) we observe similar rotations around $\mathbf{x}^*$ and boomerang turns marking transitions from clockwise to counterclockwise rotations, as shown in Figure 3(c) for $\mathcal{I}(\gamma_0)$. Figure 7(d) shows the value of $\dot{V}$ versus the arclength of $\mathcal{I}(\gamma_{30})$. This figure also helps to understand the behavior, in particular near $\mathbf{x}^*$ in panel (c); below the V-nullcline in panel (c) we have $\dot{V} > 0$, and $\dot{V} < 0$ on the other side of the V-nullcline. Note that the first two crossings of the V-nullcline in Figure 7(d) happen at points on $\mathcal{I}(\gamma_{30})$ that lie before the points shown in Figure 7(c). That is, $\mathcal{I}(\gamma_{30})$ starts from γ_{30} in Figure 7(a) in the regime $\dot{V} < 0$, and it crosses the V-nullcline at a short arclength distance from γ_{30} just before it enters a neighborhood of $\mathbf{x}^*$. The first counterclockwise loop around $\mathbf{x}^*$ is the first downward peak in Figure 7(d) after about arclength 30 of $\mathcal{I}(\gamma_{30})$.

We calculated all one hundred isochrons $\mathcal{I}(\gamma_i)$ that are shown in Figure 2 in the same way; here $\gamma_i = \Phi^{\theta_i T_\Gamma}(\gamma_0)$, where $\theta_i = \frac{i}{100}$ for $i = 0, 1, \ldots, 99$. These isochrons all have properties similar to those for $\mathcal{I}(\gamma_0)$ and $\mathcal{I}(\gamma_{30})$; namely, apart from the initial approach to $\mathbf{x}^*$, each isochron makes a series of excursions followed by boomerang turns as it converges to $\mathbf{x}^*$.

4.4. Fundamental domains of isochrons. There clearly is a strong interaction between the isochrons of the reduced Hodgkin–Huxley model (4.1) and its repelling slow manifold S_ε^r.
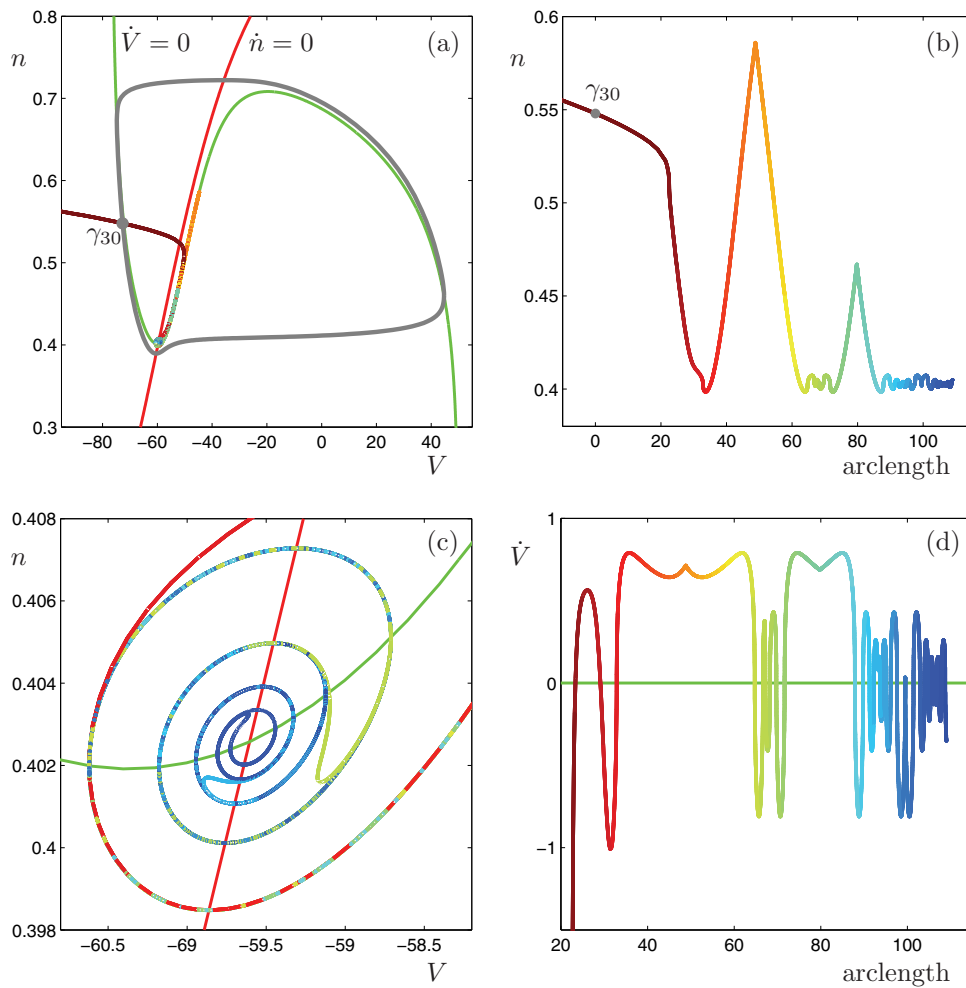
Figure 7. *The isochron $\mathcal{I}(\gamma_{30})$ of the point γ_{30} with phase $\theta_{30} = \frac{30}{100}$ on the periodic orbit (gray) of the reduced Hodgkin–Huxley model (4.1) is colored with a red-to-blue color gradient with respect to arclength distance to γ_{30}. Panel (a) shows $\mathcal{I}(\gamma_{30})$ in the phase plane, along with the V-nullcline (green) and the n-nullcline (red); panel (b) shows the n-coordinate of $\mathcal{I}(\gamma_{30})$ versus its arclength—this panel also serves as a colorbar for the figure; panel (c) is an enlargement to illustrate the accumulation onto the equilibrium $\mathbf{x}^*$ (not labeled); panel (d) shows the value of $\dot{V}$ along $\mathcal{I}(\gamma_{30})$ versus its arclength; compare also Figure 3. The associated animation (77724_06.gif [221KB]) shows a point moving along the inside branch of $\mathcal{I}(\gamma_{30})$.*

Each isochron makes a series of excursions that involve oscillations around S_ε^r. In this section we study this interaction in detail.

Let us focus again on the isochron $\mathcal{I}(\gamma_0)$ shown in Figure 3 and consider the location of the excursions of $\mathcal{I}(\gamma_{30})$, shown in Figure 7, relative to those of $\mathcal{I}(\gamma_0)$. As mentioned before, the first excursion of $\mathcal{I}(\gamma_{30})$ reaches a maximum $n \approx 0.5860$ that lies between the maxima $n \approx 0.5517$ and $n \approx 0.6802$ of the second and first excursions, respectively, of $\mathcal{I}(\gamma_0)$. Due to the steepness of the V-nullcline here, we can assume that the intersection points of $\mathcal{I}(\gamma_0)$ and $\mathcal{I}(\gamma_{30})$ with S_ε^r lie quite close to these maxima. Recall that S_ε^r is, in fact, a segment of the
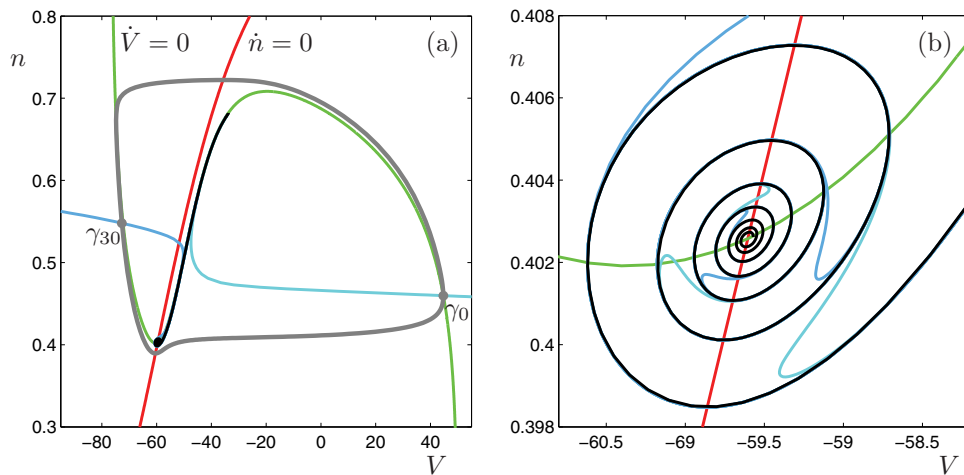
Figure 8. *The isochrons $\mathcal{I}(\gamma_0)$ (cyan) and $\mathcal{I}(\gamma_{30})$ (pale blue) of the reduced Hodgkin–Huxley equations (4.1) together with the orbit segment $\widehat{\mathbf{x}}^r$ (black) that contains the repelling slow manifold S_ε^r. Panel (a) shows the isochrons and $\widehat{\mathbf{x}}^r$ in the phase plane, and panel (b) shows an enlargement near the equilibrium $\mathbf{x}^*$ (not labeled).*

(special) orbit $\mathbf{x}^r = \mathbf{x}^r(t)$ that comes from $\mathbf{x}^*$. Let us denote the first three intersection points of $\mathcal{I}(\gamma_0)$ with $\mathbf{x}^r(t)$ by $\mathbf{r}_1$, $\mathbf{r}_2$, and $\mathbf{r}_3$, and let us assume that time along $\mathbf{x}^r(t)$ is chosen such that $\mathbf{r}_2 = \mathbf{x}^r(0)$. Then we have

$$\begin{aligned}
\mathbf{r}_1 &= \mathbf{x}^r(T_\Gamma) &= \Phi^{T_\Gamma}(\mathbf{r}_2) \quad \text{and} \\
\mathbf{r}_3 &= \mathbf{x}^r(-T_\Gamma) &= \Phi^{-T_\Gamma}(\mathbf{r}_2).
\end{aligned}$$

The first two intersection points of any isochron $\mathcal{I}(\gamma)$ with $\mathbf{x}^r(t)$ are then easily found using the phase $\theta(\gamma) = \theta$ of γ; namely, these are $\Phi^{\theta T_\Gamma}(\mathbf{r}_2)$ and $\Phi^{(\theta-1)T_\Gamma}(\mathbf{r}_2)$. Note that this holds for any $\theta \in [0,1]$. Hence, the segment between $\mathbf{x}^r(0)$ and $\mathbf{x}^r(T_\Gamma)$ defines a *fundamental domain* that consists of intersection points of *all* isochrons of Γ such that the first intersection point maps to the last intersection point under $\Phi^{T_\Gamma}(\cdot)$. The preimage of this fundamental domain is the segment between $\mathbf{x}^r(-T_\Gamma)$ and $\mathbf{x}^r(0)$. Note that *all* isochrons of Γ must pass this entire segment exponentially closely on either side in order to reach and return from the fundamental domain. In fact, we may define the entire orbit segment $\widehat{\mathbf{x}}^r := \{\mathbf{x}^r(t) \mid -\infty < t \leq 0\}$ as a curve along which *all* isochrons of Γ pass exponentially closely at least twice.

Figure 8 shows both isochrons $\mathcal{I}(\gamma_0)$ and $\mathcal{I}(\gamma_{30})$ in one figure together with an approximation of $\widehat{\mathbf{x}}^r$ (black curve). The isochron $\mathcal{I}(\gamma_0)$ is colored cyan and $\mathcal{I}(\gamma_{30})$ is colored pale blue, which are the same colors as in Figure 2. The view in panel (a) shows that large parts of the two isochrons lie very close together, virtually on top of $\widehat{\mathbf{x}}^r$. Indeed, even the enlargement in Figure 8(b) hardly distinguishes the curves; only the boomerang turns that correspond to transitions from clockwise to counterclockwise rotations are different. Moreover, both isochrons make at least two excursions along $\widehat{\mathbf{x}}^r$, and the second excursion begins and ends (well) before the first (cyan) boomerang turn of $\mathcal{I}(\gamma_0)$. Hence, what seems to be a single curve that leaves Figure 8(b) below the V-nullcline through the side $\{V = -58.2\}$ is, in fact, at least four curves, not counting $\widehat{\mathbf{x}}^r$. We can identify the segment just before the first (cyan) boomerang
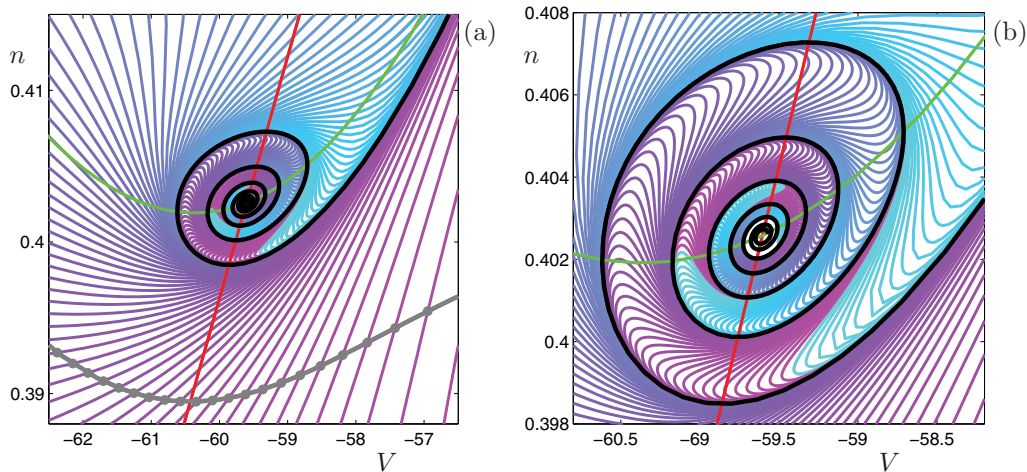
Figure 9. *A total of* 100 *isochrons (cyan-to-magenta color gradient with respect to their phases) uniformly distributed in time along the stable periodic orbit (gray) of the reduced Hodgkin–Huxley model* (4.1). *Shown are two successive enlargements near the equilibrium* $\mathbf{x}^*$ *(not labeled). The black curve represents the orbit segment* $\widehat{\mathbf{x}}^r$.

turn of $\mathcal{I}(\gamma_0)$ (which corresponds to the end of its first excursion) and the segment immediately after the first clockwise rotation of $\mathcal{I}(\gamma_0)$ around $\mathbf{x}^*$ (which corresponds to the start of its second excursion) as marking a strip on the side $\{V = -58.2\}$ through which all these curves pass.

We can give similar arguments for any isochron $\mathcal{I}(\gamma)$ with phase $\theta(\gamma) = \theta$. Indeed, $\mathcal{I}(\gamma)$ must reach the point $\Phi^{(\theta-1)T_\Gamma}(\mathbf{r}_2)$, associated with its phase θ, that lies in between $\mathbf{r}_3$ and $\mathbf{r}_2$ on $\widehat{\mathbf{x}}^r$. Moreover, in doing so it cannot intersect another isochron. Therefore, *all* isochrons must pass through the strip bounded by the first and second excursions of $\mathcal{I}(\gamma_0)$. This means that the seemingly single curve that leaves Figure 8(b) below the V-nullcline through the side $V = -58.2$ consists of infinitely many curves!

Figure 9 presents a different illustration of the phenomenon. Shown are two successive enlargements near the equilibrium $\mathbf{x}^*$ of Figure 2. The approximation of $\widehat{\mathbf{x}}^r$ (black curve) is overlaid in both panels. We observe a self-similar structure of the isochrons in this neighborhood of $\mathbf{x}^*$, and the foliation of the phase space by the isochrons appears to be organized by a contracting transformation that is reminiscent of a λ-lemma [37]; certainly, the successive points $\Phi^{-kT_\Gamma}(\mathbf{r}_2)$ contract to $\mathbf{x}^*$ in accordance with the λ-lemma.

Winfree conjectures in [45, appendix, Conjecture C] that any isochron must come arbitrarily close to any point in the phaseless set, that is, the boundary $\partial\mathcal{B}$ of the basin of attraction $\mathcal{B}(\Gamma)$ of Γ. For our example, this means that all isochrons come arbitrarily close to the equilibrium $\mathbf{x}^*$, which is the only point in the phaseless set. Figure 8 illustrates that $\widehat{\mathbf{x}}^r$, which lies in the *interior* of $\mathcal{B}(\Gamma)$, is an "almost phaseless set," because all isochrons come exponentially close to $\widehat{\mathbf{x}}^r$, rather than arbitrarily close.

Our findings are consistent with Winfree's conjecture, but they also show that extreme phase sensitivity can occur on a codimension-one set in the interior of $\mathcal{B}(\Gamma)$. To be more precise, while all isochrons are exponentially close to (the left of) the segment on $\widehat{\mathbf{x}}^r$ between

$\mathbf{x}^r(0)$ and $\mathbf{x}^r(T_\Gamma)$, they are even closer (on both sides) to the segment between $\mathbf{x}^r(-T_\Gamma)$ and $\mathbf{x}^r(0)$, and again even closer to the segment between $\mathbf{x}^r(-2T_\Gamma)$ and $\mathbf{x}^r(-T_\Gamma)$, and so on. Of course, these segments on $\widehat{\mathbf{x}}^r$ between $\mathbf{x}^r(-kT_\Gamma)$ and $\mathbf{x}^r(-(k-1)T_\Gamma)$ for $k = 1, 2, \ldots$ become successively shorter and lie successively closer to $\mathbf{x}^*$. However, the arclength of the segment between $\mathbf{x}^r(-T_\Gamma)$ and $\mathbf{x}^r(0)$ decreases with the ratio ε of the slow and fast time scales and is zero in the limit $\varepsilon \to 0$. Note that a change in the ratio between two time scales alters the slow manifold S_ε^r—it lies closer to the V-nullcline as ε decreases. For each ε we can define a corresponding orbit segment $\mathbf{x}_\varepsilon^r(t)$ such that $\mathbf{x}_\varepsilon^r(0)$ is equal to the second intersection of $\mathcal{I}(\gamma_0)$ with $\mathbf{x}_\varepsilon^r(t)$. It is important to realize that the first intersection of $\mathcal{I}(\gamma_0)$ with $\mathbf{x}_\varepsilon^r(t)$ will always be well away from $\mathbf{x}^*$; in fact, this point will move further away in arclength along $\mathbf{x}_\varepsilon^r(t)$, rather than closer to $\mathbf{x}^*$ as ε decreases. If we consider an ε-dependent family of the reduced Hodgkin–Huxley equation, then for arbitrary distance ρ and arbitrary $k \in \mathbb{N}$ we can choose $0 < \varepsilon \ll 1$ such that all isochrons will pass within distance ρ of any point on the segment $\{\mathbf{x}_\varepsilon^r(t) \mid -\infty < t \le -kT_\Gamma\}$.

5. Discussion. We have illustrated with the example of a reduced Hodgkin–Huxley model that isochrons of planar multiple-time-scale systems can be organized into a remarkably complex structure; we believe that this phenomenon is not specific to the reduced Hodgkin–Huxley model. Indeed, Winfree provides a computer-generated sketch of the isochrons of a FitzHugh–Nagumo model that show similar "boomerang turns" organized in the same way; see Box C on pages 170–172 in [46]. As predicted by the theory [21, 45], the isochrons foliate the plane, with one side extending to infinity and the other converging to the sole singularity at the equilibrium $\mathbf{x}^*$ of the reduced Hodgkin–Huxley model. However, the convergence to this phaseless set is by no means immediate. The isochrons make several "excursions" along the repelling slow manifold of the reduced Hodgkin–Huxley model. During each such excursion, the isochron passes both to the left and to the right of the repelling slow manifold, corresponding to trajectories that converge to the periodic orbit via a left or a right jump, respectively, along the fast direction of the system.

The geometry of the isochrons in a neighborhood of the equilibrium $\mathbf{x}^*$ for the reduced Hodgkin–Huxley model nicely illustrates the extreme phase sensitivity that exists in the neighborhood of a phaseless set. We found that the neighborhood of the repelling slow manifold for the reduced Hodgkin–Huxley model is also a region of phase space which will display phase sensitivity, even though it is not a true phaseless set. The structure of the isochrons near the repelling slow manifold is similar to the behavior of isochrons near a one-dimensional basin boundary, to which all isochrons come arbitrarily close [45, 21], and reminiscent of the sketch by Guckenheimer [21] showing the limiting structure of two-dimensional isochrons on the two-dimensional boundary of a three-dimensional basin of attraction. Indeed, our calculations illustrate that such structures exist in the interior of a basin of attraction as the isochrons accumulate near the repelling slow manifold; we call the repelling slow manifold an "almost phaseless set," because the density of the isochrons is not arbitrarily small but depends on the ratio $\varepsilon \ll 1$ between the slow and fast time scales of the system. (In the limit $\varepsilon \to 0$, the repelling slow manifold converges to a phaseless set.)

The isochrons are important for understanding the response properties of an oscillator to a stimulus. Local approximations to isochrons near the periodic orbit are related to the infinitesimal phase response curve, which can be interpreted as the phase shift of an oscil-

lation due to an infinitesimal, impulsive perturbation as a function of the phase at which the perturbation is applied [4, 19, 23]. Global isochrons can be used to understand phase response curves for *finite* perturbations (cf. [36]) or phase response surfaces which are useful for situations in which an oscillator is stimulated repeatedly before it relaxes back to the limit cycle attractor [22]. Winfree [45] noted that a system near a phaseless set could have its phase randomized by small noise, an idea which has recently been applied, for example in [7], to desynchronize a population of neurons; in particular, the phase of each neuron is altered randomly after the system is driven to the phaseless set using minimal-time optimal control with an amplitude-constrained input current. Our results suggest that a controller such as that considered in [7] could target the repelling slow manifold rather than the equilibrium $\mathbf{x}^*$ in order to desynchronize a population of neurons through phase randomization.

While isochrons have received the most attention in the context of biological oscillators, the concept of an isochron is also important in power electronics. Power generation systems consist of several generating units that operate in parallel. Before a new unit, for example, a wind turbine or solar panel, can be connected to a utility network, one must ensure precise amplitude, frequency, and phase conditions. In particular, phase agreement between the voltages of the generator and the power system at the instant of connection is critical because of the electromagnetic transients that follow [20, 44]. To put it in the language of isochrons, the connection of a new unit causes a perturbation of the system away from its stable periodic orbit. To ensure grid synchronization, the perturbed initial condition must lie on the isochron of the phase at the moment the connection is made. While automatic synchronization methods exist, their performance is not always reliable, and most systems use a combination of manual, semiautomatic, and automatic synchronizing schemes [42]. The reliability of automatic synchronization methods is related to the behavior of the corresponding global isochrons. This is an interesting direction for future work that ties in well with the possible extension of our techniques for higher-dimensional isochrons, as discussed below, because the primary concern is whether a perturbation with a specific voltage lies on a particular isochron.

We computed the global isochrons with a new numerical method based on two-point boundary value continuation. We view an isochron $\mathcal{I}(\gamma)$ associated with a particular phase point γ on the periodic orbit Γ as the global stable manifold of γ for the time-T_Γ map, where T_Γ is the period of Γ. Based on the method in [15], we view the isochron as a one-parameter family of orbit segments with one end point on the approximation computed so far and the other tracing new parts of the global manifold. The boundary value problem set-up uses the orbit segment that defines Γ starting at γ as the first known solution on $\mathcal{I}(\gamma)$; other solutions are found by continuation along the linear approximation of $\mathcal{I}(\gamma)$ in a prespecified small neighborhood of Γ. Each continuation step uses global information about the variation along the entire orbit segment to control the accuracy of the computation. Hence, the extreme sensitivity of initial conditions that is typical for systems with multiple time scales is spread effectively along the entire orbit segment. We implemented our method using the latest version of AUTO [11] with the Python scripting interface to select and compute automatically an arbitrary number of isochrons along a periodic orbit that are uniformly spaced in time or arclength. The adaptive step selection of AUTO ensures that the continuation generates a nicely distributed mesh along each isochron that automatically parameterizes the curves by arclength. The numerical accuracy and convergence properties of this approach allow the

computation of one-dimensional isochrons up to unprecedented arclengths.

In theory, it is straightforward to generalize the computational method presented in this paper to isochrons of three- or higher-dimensional vector fields. However, the isochrons are then two- or higher-dimensional manifolds, and their computation becomes increasingly difficult for the same reasons as in the computation of global two- or higher-dimensional stable manifolds [32]. To our knowledge, the first publication that contains computations of two-dimensional isochrons, by using backward integration methods, appeared very recently in [1]. In practice, it may be sufficient to find one-dimensional intersections of such higher-dimensional isochrons with a subspace of suitable dimension. For example, one could trace the intersection curve of a three-dimensional isochron of the four-dimensional Hodgkin–Huxley model with the hyperplane where the two additional coordinates, which are not present in our two-dimensional reduced model, are constant. The computational complexity of such an approach is comparable to the computation of one-dimensional isochrons of a planar system, but one must take into account the fact that the intersection curve of a higher-dimensional isochron may not be simply connected; see [15] for examples of such invariant manifolds.

REFERENCES

[1] H. Ben Amor, N. Glade, C. Lobos, and J. Demongeot, *The isochronal fibration: Characterization and implication in biology*, Acta Biotheor., 58 (2010), pp. 121–142.

[2] É. Benoît, J. L. Callot, F. Diener, and M. Diener, *Chasse au canards*, Collect. Math., 31 (1981), pp. 37–119.

[3] C. de Boor and B. Swartz, *Collocation at Gaussian points*, SIAM J. Numer. Anal., 10 (1973), pp. 582–606.

[4] E. Brown, J. Moehlis, and P. Holmes, *On the phase reduction and response dynamics of neural oscillator populations*, Neural Comput., 16 (2004), pp. 673–715.

[5] X. Cabré, E. Fontich, and R. de la Llave, *The parameterization method for invariant manifolds. III: Overview and applications*, J. Differential Equations, 218 (2005), pp. 444–515.

[6] A. Campbell, A. Gonzalez, D. L. Gonzalez, O. Piro, and H. A. Larrondo, *Isochrones and the dynamics of kicked oscillators*, Phys. A, 155 (1989), pp. 565–584.

[7] P. Danzl, J. Hespanha, and J. Moehlis, *Event-based minimum-time control of oscillatory neuron models: Phase randomization, maximal spike rate increase, and desynchronization*, Biolog. Cybernet., 101 (2009), pp. 387–399.

[8] M. Desroches, J. M. Guckenheimer, B. Krauskopf, C. Kuehn, H. M. Osinga, and M. Wechselberger, *Mixed-Mode Oscillations with Multiple Time Scales*, preprint, Bristol Centre for Applied Nonlinear Mathematics # BCANM.1594, University of Bristol, Bristol, UK, 2010; SIAM Rev., submitted.

[9] V. De Witte and W. Govaerts, *Convergence analysis of a numerical method to solve the adjoint linearized periodic orbit equations*, Appl. Numer. Math., 60 (2010), pp. 1007–1023.

[10] E. J. DOEDEL, *Lecture notes on numerical analysis of nonlinear equations*, in Numerical Continuation Methods for Dynamical Systems: Path Following and Boundary Value Problems, B. Krauskopf, H. M. Osinga, and J. Galán-Vioque, eds., Springer-Verlag, New York, 2007, pp. 1–50.

[11] E. J. DOEDEL, *AUTO-07P: Continuation and Bifurcation Software for Ordinary Differential Equations*, with major contributions by A. R. Champneys, F. Dercole, T. F. Fairgrieve, Yu. A. Kuznetsov, B. E. Oldeman, R. C. Paffenroth, B. Sandstede, X. J. Wang, and C. Zhang; software available via http://cmvl.cs.concordia.ca/auto/.

[12] E. J. DOEDEL, B. W. KOOI, G. A. K. VAN VOORN, AND YU. A. KUZNETSOV, *Continuation of connecting orbits in 3D-ODEs* (I): *Point-to-cycle connections*, Internat. J. Bifur. Chaos Appl. Sci. Engrg., 18 (2008), pp. 1889–1903.

[13] E. J. DOEDEL, B. W. KOOI, G. A. K. VAN VOORN, AND YU. A. KUZNETSOV, *Continuation of connecting orbits in 3D-ODEs* (II): *Cycle-to-cycle connections*, Internat. J. Bifur. Chaos Appl. Sci. Engrg., 19 (2009), pp. 159–169.

[14] F. DUMORTIER AND R. ROUSSARIE, *Canard Cycles and Center Manifolds*, Mem. Amer. Math. Soc. 121 (577), AMS, Providence, RI, 1996.

[15] J. P. ENGLAND, B. KRAUSKOPF, AND H. M. OSINGA, *Computing one-dimensional global manifolds of Poincaré maps by continuation*, SIAM J. Appl. Dyn. Syst., 4 (2005), pp. 1008–1041.

[16] B. ERMENTROUT, *Simulating, Analyzing, and Animating Dynamical Systems: A Guide to XPPAUT for Researchers and Students*, Software Environ. Tools 14, SIAM, Philadelphia, 2002.

[17] G. B. ERMENTROUT AND N. KOPELL, *Multiple pulse interactions and averaging in coupled neural oscillators*, J. Math. Biol., 29 (1991), pp. 195–217.

[18] L. GLASS AND M. C. MACKEY, *From Clocks to Chaos: The Rhythms of Life*, Princeton University Press, Princeton, NJ, 1988.

[19] W. GOVAERTS AND B. SAUTOIS, *Computation of the phase response curve: A direct numerical approach*, Neural Comput., 18 (2006), pp. 817–847.

[20] A. J. GRONO AND J. J. WLODARSKI, *Setting and testing automatic generator synchronizers*, IEEE Comput. Appl. Power, 12 (1999), pp. 38–40.

[21] J. GUCKENHEIMER, *Isochrons and phaseless sets*, J. Math. Biol., 1 (1975), pp. 259–273.

[22] A. GUILLAMON AND G. HUGUET, *A computational and geometric approach to phase resetting curves and surfaces*, SIAM J. Appl. Dyn. Syst., 8 (2009), pp. 1005–1042.

[23] B. S. GUTKIN, G. B. ERMENTROUT, AND A. D. REYES, *Phase-response curves give the responses of neurons to transient inputs*, J. Neurophysiol., 94 (2005), pp. 1623–1635.

[24] M. E. HENDERSON, *Computing invariant manifolds by integrating fat trajectories*, SIAM J. Appl. Dyn. Syst., 4 (2005), pp. 832–882.

[25] M. W. HIRSCH, C. C. PUGH, AND M. SHUB, *Invariant Manifolds*, Lecture Notes in Math. 583, Springer-Verlag, New York, 1977.

[26] A. L. HODGKIN AND A. F. HUXLEY, *A quantitative description of membrane current and its application to conduction and excitation in nerve*, J. Physiol., 117 (1952), pp. 500–544.

[27] F. C. HOPPENSTEADT AND E. M. IZHIKEVICH, *Weakly Connected Neural Networks*, Springer-Verlag, New York, 1997.

[28] E. M. IZHIKEVICH, *Dynamical Systems in Neuroscience: The Geometry of Excitability and Bursting*, MIT Press, Cambridge, MA, 2007.

[29] J. KEENER AND J. SNEYD, *Mathematical Physiology*, Springer-Verlag, New York, 1998.

[30] B. KRAUSKOPF AND H. M. OSINGA, *Growing 1D and quasi 2D unstable manifolds of maps*, J. Comput. Phys., 146 (1998), pp. 404–419.

[31] B. KRAUSKOPF AND H. M. OSINGA, *Computing invariant manifolds via the continuation of orbit segments*, in Numerical Continuation Methods for Dynamical Systems: Path Following and Boundary Value Problems, B. Krauskopf, H. M. Osinga, and J. Galán-Vioque, eds., Springer-Verlag, New York, 2007, pp. 117–154.

[32] B. KRAUSKOPF, H. M. OSINGA, E. J. DOEDEL, M. E. HENDERSON, J. GUCKENHEIMER, A. VLADIMIRSKY, M. DELLNITZ, AND O. JUNGE, *A survey of methods for computing (un)stable manifolds of vector fields*, Internat. J. Bifur. Chaos Appl. Sci. Engrg., 15 (2005), pp. 763–791.

[33] B. KRAUSKOPF AND T. RIESS, *A Lin's method approach to finding and continuing heteroclinic connections involving periodic orbits*, Nonlinearity, 21 (2008), pp. 1655–1690.

[34] J. MOEHLIS, *Canards for a reduction of the Hodgkin-Huxley equations*, J. Math. Biol., 52 (2006), pp. 141–153.

[35] H. M. OSINGA AND G. R. ROKNI LAMOOKI, *Numerical study of manifold computations*, in Proceedings of the International Conference on Differential Equations (Equadiff 2003), F. Dumortier, H. W. Broer, J. Mawhin, A. Vanderbauwhede, and S. Verduyn Lunel, eds., Hasselt, World Scientific, Singapore, 2005, pp. 190–195.

[36] S. A. OPRISAN, A. A. PRINZ, AND C. C. CANAVIER, *Phase resetting and phase locking in hybrid circuits of one model and one biological neuron*, Biophys. J., 87 (2004), pp. 2283–2298.

[37] J. PALIS AND W. DE MELO, *Geometric Theory of Dynamical Systems*, Springer-Verlag, Berlin, 1982.

[38] T. PAVLIDIS, *Biological Oscillators: Their Mathematical Analysis*, Academic Press, New York, 1973.

[39] F. SCHILDER, H. M. OSINGA, AND W. VOGT, *Continuation of quasi-periodic invariant tori*, SIAM J. Appl. Dyn. Syst., 4 (2005), pp. 459–488.

[40] W. E. SHERWOOD AND J. GUCKENHEIMER, *Dissecting the phase response of a model bursting neuron*, SIAM J. Appl. Dyn. Syst., 9 (2010), pp. 659–703.

[41] C. SIMÓ, *On the analytical and numerical approximation of invariant manifolds*, in Les Méthodes Modernes de la Mécanique Céleste (Goutelas, 1989), D. Benest and C. Froeschlé, eds., Editions Frontieres, Gif-sur-Yvettes, 1990, pp. 285–330.

[42] W. M. STRANG, C. J. MOZINA, B. BECKWITH, T. R. BECKWITH, S. CHHAK, E. C. FENNELL, E. W. KALKSTEIN, K. C. KOZMINSKI, A. C. PIERCE, P. W. POWELL, D. W. SMAHA, J. T. UCHIYAMA, S. M. USMAN, AND W. P. WAUDBY, *Generator synchronizing industry survey results*, IEEE Trans. Power Delivery, 11 (1996), pp. 174–183.

[43] D. TAKESHITA AND R. FERES, *Higher order approximation of isochrons*, Nonlinearity, 23 (2010), pp. 1303–1323.

[44] A. TIMBUS, R. TEODORESCU, F. BLAABJERG, AND M. LISERRE, *Synchronization methods for three phase distributed power generation systems. An overview and evaluation*, in Proceedings of the 36th IEEE Power Electronics Specialists Conference (PESC '05), Recife, 2005, Piscataway, NJ, pp. 2474–2481.

[45] A. T. WINFREE, *Patterns of phase compromise in biological cycles*, J. Math. Biol., 1 (1974), pp. 73–93.

[46] A. T. WINFREE, *The Geometry of Biological Time*, 2nd ed., Springer-Verlag, New York, 2001.